**Taphonomic bias on calcareous micro and nannofossils and paleoenvironmental evolution across the Messinian Salinity Crisis onset:
Insights from the Sorbas Basin (SE Spain).**

Taphonomic bias on calcareous micro and nannofossils and paleoenvironmental evolution across the Messinian Salinity Crisis onset: insights from the Sorbas Basin (SE Spain)

Mancini[a], A. M., Gennari[a], R., Natalicchio[a], M., Dela Pierre[a], F., Carnevale[a], G., Pastero[a], L., Pellegrino[a], L., Pilade[a], F., Lozar[a], F.

[a] Dipartimento di Scienze della Terra, Università degli Studi di Torino, Via Valperga Caluso 35, 10125 Torino, Italy.

Corresponding author: alanmaria.mancini@unito.it

Abstract

During the Messinian Salinity Crisis (MSC, 5.97-5.33 Ma) the synergy between tectonic and climatic processes promoted the deposition of evaporites throughout the Mediterranean Basin. The disappearance of calcareous nannofossils and foraminifers at the MSC onset has been traditionally interpreted as the result of the establishment of hypersaline conditions in the water column, which were lethal for most marine eukaryotes. Here, we investigate the calcareous micro and nannofossil assemblages from the Sorbas Basin (SE Spain) spanning the onset and the first phase of the MSC (~ 5.9-5.7 Ma) in order to test whether their disappearance was related to adverse environmental conditions and/or to preferential dissolution of biogenic calcite. Micropaleontological analyses and petrographic observations suggest that the disappearance of calcareous fossils was the result of a taphonomic bias related to paleoceanographic changes that favoured the oxidation of both pyrite and organic matter at the sea floor. A poorly preserved benthic and planktic assemblage and aragonitic laminated sediment characterize the deposits of the first phase of the MSC from 5.93 Ma onward; aragonite deposition was likely bio-mediated in response to enhanced photosynthesis, as suggested by its $\delta^{13}C$ signature. The fossil assemblage preserved in these deposits indicates a shallowing upward trend of the basin with respect to the pre-evaporitic phase, and the establishment of a lagoon-like environment characterized by episodic improvement of the connections with the open sea. We conclude that the temporary disappearance of calcareous fossils approximately at the MSC onset was related to ongoing basin restriction, which increased the sensitivity of the basin to fresh-water input and temperature changes, promoting marked fluctuations of the redox conditions in bottom sediments. This finding challenges the view of a marine biotic crisis related to hypersaline conditions at the MSC onset and opens new perspectives on the paleoenvironmental conditions that characterized this time interval.

1- Introduction

The Messinian Salinity Crisis (MSC) is commonly regarded as the most extreme event that affected the Mediterranean region during its recent geological history (e.g. Hsü et al., 1977). This event was promoted by the tectonically-driven restriction of the connection between the Mediterranean Basin and

the Atlantic Ocean (Flecker et al., 2015; Capella et al., 2018; Corbí et al., 2020), eventually leading to widespread evaporite deposition in the marginal and deep Mediterranean basins. Such a restriction proceeded by steps (Kouwenhoven et al., 1999; Vasiliev et al., 2019; Kontakiotis et al., 2019; Corbí et al., 2020; Zachariasse et al., 2021; Kontakiotis et al., 2022), as indicated by the sedimentary and fossil records (Kouwenhouven et al., 2006; Mancini et al., 2020). These restriction steps decreased both the water exchange between the Mediterranean and the Atlantic Ocean and the bottom water circulation in the Mediterranean Basin (Kouwenhouven et al., 1999; Bulian et al., 2022). The last step preluding the onset of the crisis is marked by the recently described MSC onset bioevent (5.99 Ma; Lozar et al., 2018; Lozar and Negri, 2019; Mancini et al., 2020), consisting of a succession of peaks of abundance of certain calcareous nannofossil (CN) taxa, such as *Sphenolithus abies*, followed or accompanied by abundance peaks of *Helicosphaera carteri*, *Umbilicosphaera rotula* and *Rhabdosphaera clavigera* (Lozar et al., 2018; Gennari et al., 2018; Lozar and Negri, 2019). According to Mancini et al. (2020), this event was probably triggered by the restriction of the Mediterranean basin which became more sensitive to continental freshwater input.

During the MSC, increased seawater salinity was thought to be responsible for both gypsum and halite deposition and for the establishment of a biotic crisis, with consequent gradual diversity decline and final disappearance of most marine eukaryotes (Blanc-Valleron et al., 2002; Rouchy and Caruso, 2006; Drinia et al., 2007; Moisette et al., 2018; Zachariasse et al., 2021; Kontakiotis et al., 2022). Indeed, the MSC onset is often marked by the disappearance of foraminifers and CN in many Mediterranean successions; such bioevent has been traditionally used as an indirect biostratigraphic marker that best approximates the MSC onset (e.g. Sprovieri et al. 1996, Blanc-Valleron et al. 2002; Manzi et al. 2007, Gennari et al., 2013; Violanti et al., 2013; Gennari et al., 2018; Manzi et al., 2016; Manzi et al., 2018). However, the diachronous nature of the disappearance of CN and foraminifers with respect to the MSC onset was observed in sections of the Piedmont and Sicily basins (Violanti et al., 2013; Dela Pierre et al., 2014; Catalano et al., 2016; Sabino et al., 2020; Gennari et al., 2020). Interestingly, in the Piedmont sections the disappearance of CN and foraminifers is associated with the disappearance of reworked specimens of CN and foraminifers (i.e. from older stratigraphic intervals such as Paleogene and Cretaceous) (Dela Pierre et al., 2014; Lozar et al., 2018; Gennari et al., 2020), although sediment reworking is well recorded after the onset of the MSC (e.g. Natalicchio et al., 2019; Sabino et al., 2020) and should have led to the presence of reworked calcareous tests as well. In this light, the absence of calcareous tests, including those reworked from older stratigraphic levels, may be related to diagenetic processes causing the preferential dissolution of biogenic calcite, thereby suggesting that the disappearance of marine calcareous fossils was not caused by the establishment of lethal environmental conditions in the water mass and at the seafloor (Dela Pierre et al., 2014; Gennari et al., 2020). Furthermore, several evidences based on fossil occurrence during the Primary Lower Gypsum (PLG) phase (i.e. CN, foraminifers, molecular fossils, diatoms, fishes, and

echinoids; Landini and Sorbini, 1989; Lacour and Néraudeau, 2000; Néraudeau et al., 2002; Carnevale et al., 2019; Pellegrino et al., 2021) argue against a biotic crisis associated with the MSC onset. Although the MSC time interval coincides with the absence of foraminifers (i.e. Non Distinctive Zone, recently reviewed by Lirer et al., 2019), in SE Spain (Sorbas and Bajo Segura Basins), calcareous micro and nannofossils were recorded in the marly hemicycles of the PLG unit (Van de Poel, 1992; Riding et al., 1998; Goubert et al., 2001; Corbí and Soria, 2016). Such fossils were considered as autochthonous, since evidence of reworking (e.g. abrasion, dissolution and fragmentation of the tests) were not recognised (Corbí et al., 2016).

In order to shed light on the cause of the disappearance of the calcareous fossils at the onset and during the first phase of the MSC, as well as on the paleoenvironmental conditions during this critical interval of the Mediterranean history, we studied a composite section in the Sorbas Basin (Spain), encompassing the pre-evaporitic to evaporitic transition and the PLG, in the frame of a well-established astrochronologic age model (Krijgsman et al., 1999; Sierro et al., 2001; Krijgsman et al., 2001; Manzi et al., 2013). Our reconstructions were based on detailed analyses of the micropaleontological assemblages of laminated marl, marlstone, clay and carbonate layers recording the pre-MSC/MSC transition and of the marly interbeds of the PLG unit. Micropaleontological investigations on abundance and preservation of CN and foraminiferassemblages were complemented by mineralogical, petrographic, element composition and carbon and oxygen stable isotope analyses of the same sediments.

2- Geological setting

The Sorbas Basin is a small and narrow Neogene Basin surrounded by elongated basement ridges forming the Sierra the Los Filabres, Sierra Alhamilla and Sierra Cabrera (Fig. 1). The Messinian stage in the Sorbas Basin is recorded by the Caños Formation, which is subdivided into four members: the Abad, Yesares, Sorbas and Zorreras members (Ruegg, 1964; Volk, 1967). The Abad Member was deposited in the basin depocenter (estimated paleodepth of 400±100 m; Krijgsman et al., 2006) and records the Tortonian/Messinian boundary at its base (Sierro et al., 2001); toward the northern and southern basin margins, the sediments of the Abad Member pass to reefal limestone (Roveri et al. 2009). The Abad Member is divided into two units showing a precession-driven cyclical stacking pattern: the Lower Abad (LA), characterized by the alternation of white and grey marls, and the Upper Abad (UA), characterized by the alternation of sapropel and diatomite layers sandwiched between white massive marls (Sierro et al., 2001; 2003). The Abad Member is overlain by the Yesares Member through a sharp but stratigraphically continuous boundary (Manzi et al., 2013; Mancini et al., 2020), which was interpreted by some authors as an erosional surface (Riding et al., 1998; Braga et al., 2006; Bourillot et al., 2009). The Yesares Member corresponds to the local equivalent of the PLG

unit (Roveri et al., 2014) and is characterized by up to 16 lithological cycles composed of laminated marl and gypsum or carbonate couplets (Dronkert et al., 1976; Krijgsman et al., 2001; Lugli et al., 2010; Roveri et al., 2020); the base of the first gypsum bed marks the MSC onset at 5.971 Ma (Manzi et al., 2013). Gypsum and carbonates are thought to reflect relatively more arid climate at precession maxima, whereas marls were deposited during more humid phases at precession minima (Krijgsman et al., 2001). A palaeodepth of ~ 150 - 240 m at the base of the Yesares gypsum has been estimated based on benthic foraminifers (BF) and considering the difference of elevation between the top of the uppermost pre-MSC reef layer and the first gypsum bed (Dronkert, 1976; Troelstra et al., 1980; van de Poel, 1992; Riding et al., 1998; Baggley, 2000; Clauzon et al., 2015; Modestou et al., 2017). An oolite and microbialite-dominated carbonate platform, referred to as the Terminal Carbonate Complex (TCC, Fortuin and Krijgsman, 2003; Roveri et al., 2009; Clauzon et al., 2015), represents the shallow water marginal equivalent of the Yesares Member (Roveri et al., 2020). The transition between the Yesares and Sorbas members reflects a shallowing upward trend responsible for the establishment of coastal environments in most parts of the Sorbas Basin (Krijgsman et al., 2001) and the eastward progradation of deltaic and coastal wedges along the basin axis, with lagoon and beach deposits at the top (Roep et al., 1998). Based on sedimentological observations, the palaeodepth of the basin at the Yesares/Sorbas members transition can be estimated at 75 to 100 m (Krijgsman et al., 2001; Roveri et al., 2020). The Sorbas Member underlies the continental deposits of the Zorreras Member, which consists of reddish silts and interbedded lacustrine limestones. The Zorreras Member represents the local expression of the last stage of the MSC (5.55-5.33 Ma), and also records the Messinian/Zanclean boundary (Roveri et al., 2019).

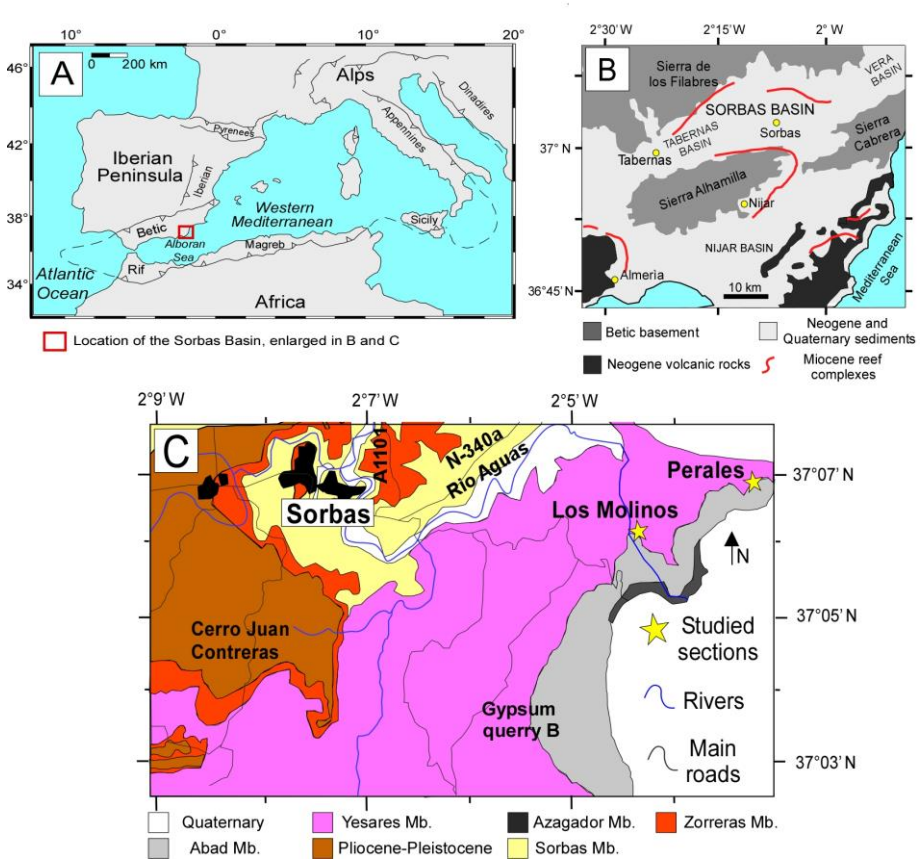

Fig. 1: A: Location of the Sorbas Basin in the Mediterranean region (modified from Corbí and Soria, 2016). B: Simplified geological map of SE Spain showing the location of the Sorbas Basin (modified from Buorrillot et al., 2009). C: Geological map of the Sorbas Basin and location of the studied sections (modified from Roveri et al., 2020)

3- Material and methods

3.1. Studied sections and sampling

3.1.1 Perales section

The Perales section (37°05′49″N; 2°03′19″W) records the complete succession of events from the base of the Messinian (Abad Member, Sierro et al., 2001) to the lower 2 PLG cycles (Yesares Member, Manzi et al., 2013). The UA is characterized by quadripartite lithological cycles (laminated sapropel, lower homogeneous marl, diatomite, upper homogeneous marl) deposited under precessional control and under specific oceanographic and environmental conditions (stage 1 to 4 of Sierro et al., 2003; Mancini et al., 2020). An important lithological change is recorded in the uppermost pre-evaporitic cycle UA34, in which the "classical" lithological cycles that characterize the UA are replaced by brown organic rich marls with alternating poorly and finely laminated intervals, intercalated by a spiculite layer and two limestone beds (Fig. 2); therefore, the thickness of the organic rich marls in the cycle UA34 is greater compared to the underlying cycles. Calcareous fossils

sharply disappear in the uppermost limestone layer (Mancini et al., 2020), which is followed by a blue/grey clay interval. This thick (2.7 meters) and anomalous lithological cycle precedes the lowermost PLG cycle, made up of dark brown laminated marl and a laterally discontinuous gypsum layer up to 3 m thick. The base of this layer is interpreted to correspond to the onset of the MSC in the Perales section (Manzi et al., 2013). The gypsum bed of cycle PLG2, 7 to 10 meters thick, is composed of laminated marl and laterally continuous massive selenite. Samples of the pre-MSC interval up to PLG1 are the same reported in Mancini et al., (2020).

3.1.2 Los Molinos section

The Los Molinos section (37°5'53''N; 2°4'39''W) is located to the North of the Los Molinos de Rio Aguas village (Fig. 1) along a canyon cut into the gypsum beds of the Yesares Member that comprises different gypsum lithofacies (i.e. massive, banded and branching selenite; Lugli et al., 2010). The marly hemicycles of the PLG unit are composed of laminated silty marl, marlstone (consolidated laminated silty marl) and limestone (Fig. 2; supplementary material Fig. 1). No erosional contacts were observed in the field. The thickness of the gypsum beds decreases upward, as observed in the PLG unit of other Mediterranean sub-basins (Lugli et al. 2010). The section starts from the second PLG cycle, but the total number of cycles is controversial, ranging from 13 (Dronkert et al., 1976) to 15 (Krijgsman et al., 2001) or 16 (Roveri et al., 2009). This inconsistency raises from the different interpretation of the upper part of the section, in which the recognition of the lithological cyclicity is not straightforward. Indeed, in cycle PLG11 the laminated marls are replaced by micritic limestones with unusual thickness (5 meters) compared to the other marly PLG hemicycles (commonly 1.5 – 2 meters) (Fig. 2). Krijgsman et al. (2001) subdivided such thick micritic limestone interval into three precessional cycles; Roveri et al. (2009) confirmed this interpretation on the basis of the presence of discontinuous gypsum layers within the micritic limestone interval. Since we did not recognise neither any significant lithological and colour change, nor any gypsum layer in the micritic limestone interval, we considered this interval as representing a single hemicycle (Fig. 2). In addition, the counting of the PLG cycles in the upper part of the section was also hampered by the vegetation cover and by the thinning of the gypsum beds, often present as isolated outcrop spots. In this section we collected 61 samples in the marl/limestone hemicycles (Fig. 2). We were unable to sample cycle PLG10 because the outcrop was not accessible.

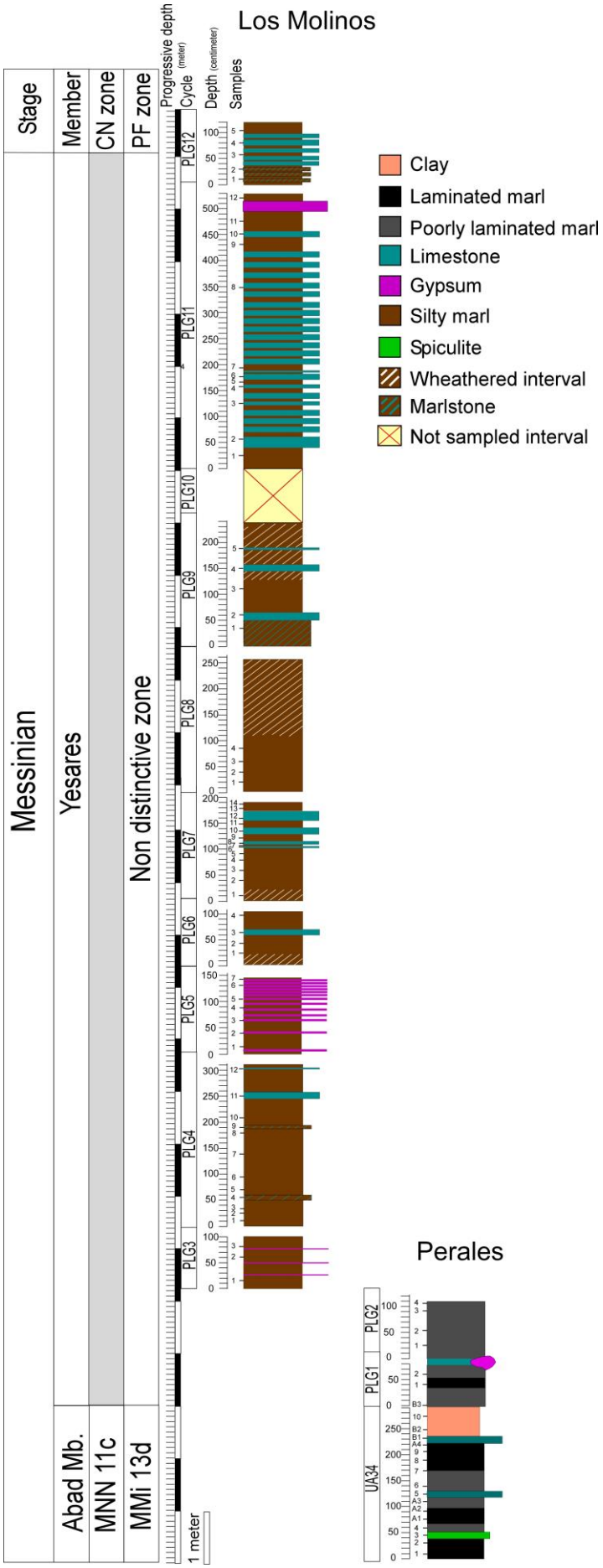
Los Molinos
Stage
Member
CN zone
PF zone
Messinian
Yesares
Abad Mb.
MNN 11c
MMi 13d
Non distinctive zone
Progressive depth (meter)
Cycle
Depth (centimeter)
Samples
PLG12
PLG11
PLG10
PLG9
PLG8
PLG7
PLG6
PLG5
PLG4
PLG3
1 meter
Clay
Laminated marl
Poorly laminated marl
Limestone
Gypsum
Silty marl
Spiculite
Wheathered interval
Marlstone
Not sampled interval
Perales
UA34
PLG1
PLG2

Fig. 2: Composite stratigraphic column of the studied succession. Cycle PLG10 was not sampled.

3.2 Calcareous nannofossils analysis

A total of 97 samples of laminated marls, marlstones, clays, and limestones (Fig. 2) were processed with the standard smear slides technique (Bown and Young, 1998) for the CN relative abundance study. Particular attention was paid to the smear slide preparation procedure in order to avoid contamination between samples, since the presence/absence of even small amounts of CN is a relevant parameter in this study. Excluding completely barren samples, at least 400 CN specimens were identified and counted at 1250× by polarized light microscopy in each slide; the reworked species from older stratigraphic interval were counted separately and thereafter included in the total CN counted. The taxa *S. abies* and *Sphenolithus moriformis* were grouped together in the informal group *Sphenolithus* gr. Since the marine fossil record in PLG deposits was often considered as the result of reworking from older sediments (Trenkwalder et al., 2008; Karakitsios et al., 2017), our analysis aimed at assessing the potential reworked nature of the CN and, more generally, of the entire micropaleontological assemblage. Accordingly, we assume that the presence of intact coccosphere and/or the preservation of dissolution prone species (i.e. *Syracosphaera pulchra*, *Pontosphaera* sp., according to Roth and Berger, 1975; Roth and Coulbourn, 1982; Gibbs et al., 2004) are likely indicative of *in-situ* assemblages, suggesting moderate or no reworking.

3.3 Microfossil analysis

A total of 57 samples of laminated marls, marlstones, clays and limestones from the Los Molinos and Perales sections (Fig. 2) were prepared for microfossil (benthic and planktic foraminifers and ostracods) investigation at the light microscope. About 100 g of oven-dried sediment were soaked in diluted H_2O_2 for 1 day, and dry-sieved to obtain 3 different size fractions: > 500 µm, 500 – 125 µm and 125 – 63 µm. Since foraminifer abundance and preservation were often scarce, we described samples by means of qualitative observations separately on the 125 - 500 µm and 63 - 125 µm residues.

3.4 Petrographic and mineralogical analyses

A total of 11 thin sections were obtained from epoxy impregnated samples cut parallel and perpendicular to the bedding. Optical microscope observations of the thin sections were performed using an Olympus BX51. Two representative thin sections of laminated samples were observed using a Nikon microscope equipped with a B-2a filter block (illumination source with an excitation wavelength of 450–490 nm). The thin sections were carbon coated and analyzed with a JMS-IT300LV Scanning Electron Microscope (SEM). Semi-quantitative characterization of the main

elements was performed during SEM investigation using an energy-dispersive EDS Oxford Instrument Link System microprobe. Elemental compositional maps were obtained from selected area using the software Inca (acquisition time one hour, Cts > 130000). Additionally, one or two representative stubs from freshly broken sediment chips from each precessional cycle were prepared for morphological investigations. Morphological investigations were also performed on hand-picked microfossils (benthic and planktic foraminifers and ostracods).

The laminated sediments from cycles PLG4 and PLG7 show alternation of white and brown laminae; the white laminae from 11 samples were scraped using a tiny needle and then powdered using an agate mortar. Powders of limestone beds belonging to the PLG6, PLG7, PLG9 and PLG11 were obtained as well using the same procedure. The powders were successively analyzed with X-Ray Powder Diffraction (XRPD). Measurements for the raw identification of the crystalline phases were carried out using a Rigaku MiniFlex 600 benchtop X-ray diffractometer (Bragg-Brentano geometry, CuKα radiation, X-ray source operating at 600W (40 kV, 15 mA); D/teX Ultra2 silicon strip detector; $2° < 2\theta < 50°$, step width 0.01°, scan speed 5 °/min).

3.5 Carbon and oxygen stable isotope analyses

An aliquot (~ 300 µg) of the same powder samples prepared for XRPD analyses was used for stable oxygen and carbon isotope analyses using an automated carbonate preparation device (Gasbench II) and a Thermo Fisher Scientific Delta V Advantage continuous flow mass spectrometer. Carbonate powder samples were reacted with > 99% orthophosphoric acid at 70°C. The carbon and oxygen isotope bulk compositions are expressed in the conventional delta notation calibrated to the Vienna Pee-Dee Belemnite (V-PDB) scale by the international standards IAEA 603 and NBS-18. Analytical reproducibility for these analyses was better than ± 0.1‰ for both $\delta^{18}O$ and $\delta^{13}C$ values.

4- Results

4.1 Calcareous nannofossils

4.1.1 Perales section

Calcareous nannofossil content of the pre-MSC sediments from the Perales section and its paleoenvironmental meaning were described in detail in Mancini et al. (2020). Cycle UA34 records the MSC onset bioevent, coinciding with a relevant increase in the CN absolute abundance (Mancini et al., 2021). Above this bioevent the assemblage is dominated by *Coccolithus pelagicus* and *Reticulofenestra pseudoumbilicus* (supplementary material Fig. 4). The preservation of CN from the MSC onset bioevent to the base of cycle PLG1 progressively decreases, as highlighted by dissolution features (e.g. etching) affecting coccoliths (mostly *Helicosphaera carteri* and *C. pelagicus*). From the

second limestone bed of cycle UA34 (Fig. 2) up to cycle PLG2, CN are absent. Interestingly, reworked specimens from older stratigraphic intervals, usually present in the UA cycles with variable percentages (0.4 -23.6 %, average = 4.6 %; supplementary material Fig. 4), were not observed in the barren samples of this interval.

4.1.2 Los Molinos section

In the Los Molinos section, CN are present in 36 out of 61 samples. The abundance and diversity of the CN are generally lower than in the UA samples, except for a few samples with higher concentration and a more diversified assemblage in cycles PLG4, PLG6, PLG7 and PLG9 (Fig. 3). The CN preservation is generally poor, as revealed by dissolution features affecting coccoliths, such as etching affecting the external rim and central area and fracturing (Fig. 4c, supplementary material Fig. 8c). Overall, the CN assemblage is dominated by *Reticulofenestra minuta,* followed by other reticulofenestrids, *H. carteri*, *Sphenolithus* gr. and *C. pelagicus*. *Umbilicosphaera rotula* and *Umbilicosphaera jafari* are present with moderate to low abundance. The abundance of reworked specimens is generally low (2% on average) and rarely exceeds 5%. In one sample (PLG4 sample 2), both dissolution prone CN and intact coccospheres (*R. minuta, R. haqii, U. jafari, H. carteri, C. pelagicus*) are present (Fig. 3).

It is worth noting that all the samples devoid of possible *in situ* assemblages are also characterized by the absence of reworked specimens. In particular, samples from cycles PLG1, PLG2, PLG5 and PLG8 are completely barren of both synsedimentary and reworked CN.

4.2 Microfossils

We include in this chapter qualitative and semi-quantitative analyses of foraminifer specimens observed in washing residues at the optical microscope and at the SEM.

4.2.1 Perales section

Approximately from cycle UA27 upward (~ 6.15 Ma), the planktic foraminifers show a substantial decrease in the preservation state, with an increase of the specimens affected by encrustation and dissolution of external wall and by sediment/mineral infills (Reghizzi et al., 2017; Mancini et al., 2020). Similar features were also observed in the Eastern Mediterranean from the Tortonian/Messinian boundary to the MSC onset (Crete Island, Antonarakou et al., 2019). According to the nomenclature adopted to describe the preservation state of planktic foraminifers (PF) proposed by Antonarakou et al. (2019), from cycle UA27 to cycle UA34 the PF assemblage is dominated by "chalky" specimens. Planktic foraminifers disappear below the first limestone bed of cycle UA34 (sample A3, Fig. 5), slightly below BF (Fig. 5). Benthic foraminifers are present up to the second limestone bed of cycle UA34; within this cycle, they are exclusively represented by low-oxygen tolerant bolivinids (*Bolivina spathulata* and *Bolivina dilatata*) and buliminids (*Bulimina aculeata* and

Bulimina elongata), among which *Bolivina dilatata* is dominant. From cycle UA27 upward, the shells of BF are characterized by a progressive increase in dissolution, recrystallization and encrustation features clearly visible at the SEM compared to BF recorded in the lower cycles (supplementary material Fig. 2 and Fig. 3). SEM observations show the presence of abundant pyrite or oxidised pyrite inside the foraminifer shell (Fig. 5 A3; supplementary material Fig. 3). In some cases, oxidised pyrite was found to occupy a small void deriving from the BF shell dissolution (Fig. 5A4). From the second limestone bed upward, foraminifers have not been observed in the washing residues.

4.2.2 Los Molinos section

In the Los Molinos section, foraminifers (both 63 - 125 and > 125 µm size fraction) are generally rare (PLG4, PLG7, PLG11 and PLG12) or absent (PLG3, PLG5 and PLG8) except in cycles PLG6 and PLG9 where some layers yield more abundant BF (Fig. 3). Preservation is generally scarce, with specimens showing partial dissolution of the outer side of the wall, fragmentation and external encrustation; pyrite framboids or oxidised pyrite infills were also observed (supplementary material Fig. 8). According to the definition of preservation classes proposed by Antonarakou et al. (2019), the recorded foraminifers are mostly "chalky". In some cases, the external encrustation of the tests hampered the taxonomic identification at the species or even at genus level. Reworked taxa from older stratigraphic interval were not recorded throughout the section. Detrital grains and bioclastic materials are almost absent in the 63 – 125 µm size fraction.

In cycle PLG4, the >125 µm fraction of each sample is barren, while rare bolivinids, *Turborotalita quinqueloba* and globigerinids are present in the smaller fraction of samples collected in the lower half of the marly hemicycle (Fig. 3). All the samples of cycle PLG5 were barren of foraminifers in both the size fractions. The basal sample of cycle PLG6 yields very rare and badly preserved BF in the smaller-size fraction. Rare to common *Fursenkoina fusiformis* specimens are observed in the middle of the marly interval of cycle PLG6 (Fig. 3), where the assemblage is nearly monospecific, although some specimens of *B. aculeata* are also present in the <125 µm size fraction. Just above, only few *Cribroelphidium* specimens and small bolivinids were observed. In cycle PLG7, barren samples alternate with samples yielding rare *Globigerinoides* spp. and BF that are variably represented by species of *Ammonia*, *Cribroelphidium*, *Bulimina* and *Bolivina* in both size fractions (Fig. 3). Usually, the assemblages are oligospecific, except in cycle PLG7 (sample 13), where species of these genuses co-occur. The samples from the marly interval of cycle PLG9, yield rare to common miliolids, sometimes associated with disarticulated valves of the ostracod *Cyprideis* sp. (Fig. 3). Cycles PLG11 yield prevalently barren samples, except in three samples in which common to rare PF (*Globigerinoides* spp., *T. quinqueloba* and neogloboquadrinids) were observed; on the other hand, benthic assemblage was recorded only in the uppermost sample in the >125 µm size fraction (Fig. 3). Cycle PLG12 is barren of microfossils (Fig. 3)

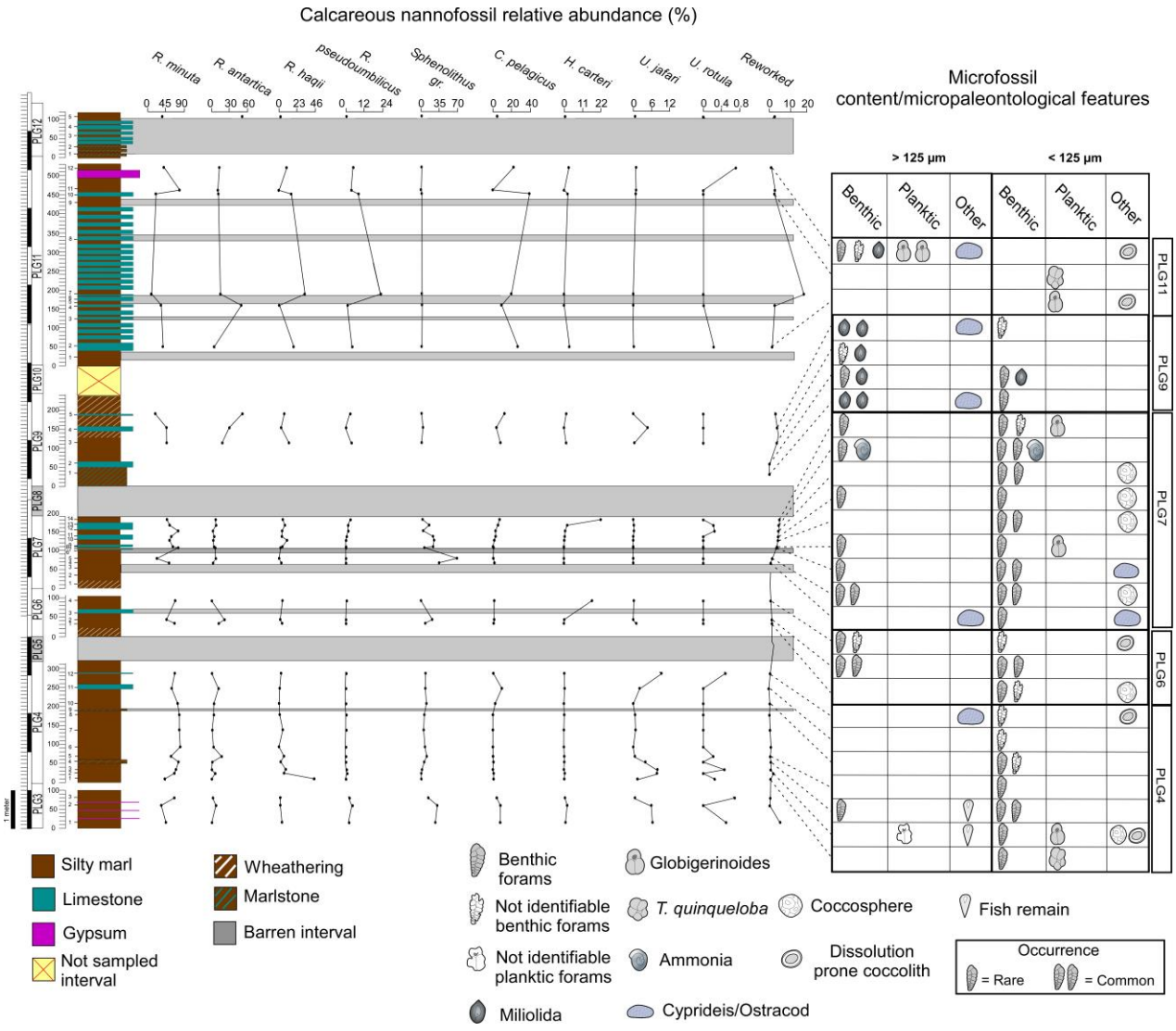

Fig. 3: Micro and nannofossil content of Los Molinos section. Bolivinids, Buliminids, Uvigerinids, *Elphidium*, *Cibroelphidium* and *Fursenkoina* are grouped together and plotted as benthic foraminifers. Cycles PLG5 and PLG8 are barren of fossils; cycle PLG10 was not sampled.

4.3 Petrographic and taphonomic observations

SEM observations of polished thin sections and stubs allowed further characterization of the samples collected from cycles UA34 to PLG12. Pyrite has been found within and on the wall of certain individual of BF specimens, as well as in the sedimentary matrix (supplementary material Fig. 8E and Fig. 9B), which consists of clay, silt-sized terrigenous grains or micrite. Pyrite observed in the matrix is consistently small-sized (< 10 µm; supplementary material Fig. 8E, Fig. 9B and Fig. 9F). Pyrite and oxidised pyrite moulds (most likely after PF and BF) are present in cycle UA34 (Fig. 5 A3

and $A3_2$); these features increase in abundance upward in the section, becoming very common in the second limestone bed of cycle UA34 (Fig. 5 B1, $B1_2$ and $B1_3$), although no PF, CN and BF were observed through optical microscope observations of smear slides and washing residues. In some cases, the calcitic test of foraminifers is either completely dissolved or replaced by calcite microcrystals (Fig. 5 $B1_2$ and $B1_3$). Sparry calcite filling the foraminifer chambers was also rarely observed (Fig. 5 $B1_3$). This limestone bed is overlain by a blue/grey clay bed characterized by very low abundance of carbonate grains (supplementary material Fig. 6), as revealed by EDS analyses. Sub-spherical Si-rich grains with a circular cross section (300 to 800 µm in diameter) surrounded by a siliciclastic matrix were observed in this level. Rounded cavities with oxidised pyrite infill are also present (Fig. 5 $B2_2$). Above the clay bed, the laminated marly hemicycle of cycles PLG1 and PLG2 still contains pyrite and oxidised pyrite aggregates, some of them with elongated shape resembling normal size to dwarfed BF internal moulds (Fig. 5 B3).

The Los Molinos section is characterized by prevalently laminated silty marls with poorly preserved calcareous fossils (CN, ostracods and foraminifers; Fig. 3 and Fig. 4 B, C, D, E and F; supplementary material Fig. 8 A, B, C, D, E and F), although some levels were completely barren (Fig. 3). The marly hemicycles of cycles PLG4 and PLG7, which yield rare to common BF, show peculiar features as they host laminated silty marl typified by the alternation of sub-mm thick brown and white laminae (Fig. 6). EDS analyses show that the brown laminae contain aluminosilicates composed of Mg, Si, Al and K (Fig. 7). Calcareous nannofossils, aragonite (as revealed by XRPD analysis), calcite and pyrite grains <5 µm are also present in these laminae as minor components. In contrast, the white laminae are almost exclusively composed of aragonite, based on XRPD results (supplementary material Fig. 7) (about 70% – 90% based on SEM qualitative observation), with CN and pyrite grains <5 µm as a minor component. Aragonite crystals commonly show two habits: bladed crystals, about 10 µm long, and acicular needles usually < 6 µm. Bladed aragonite sometimes is locally grouped to form clusters of radially oriented crystals (supplementary material Fig. 9). The aragonitic laminae display 1 – 5 µm large longitudinal cracks (Fig. 6 and Fig. 7). Celestite and barite were also sporadically observed within the aragonitic laminae.

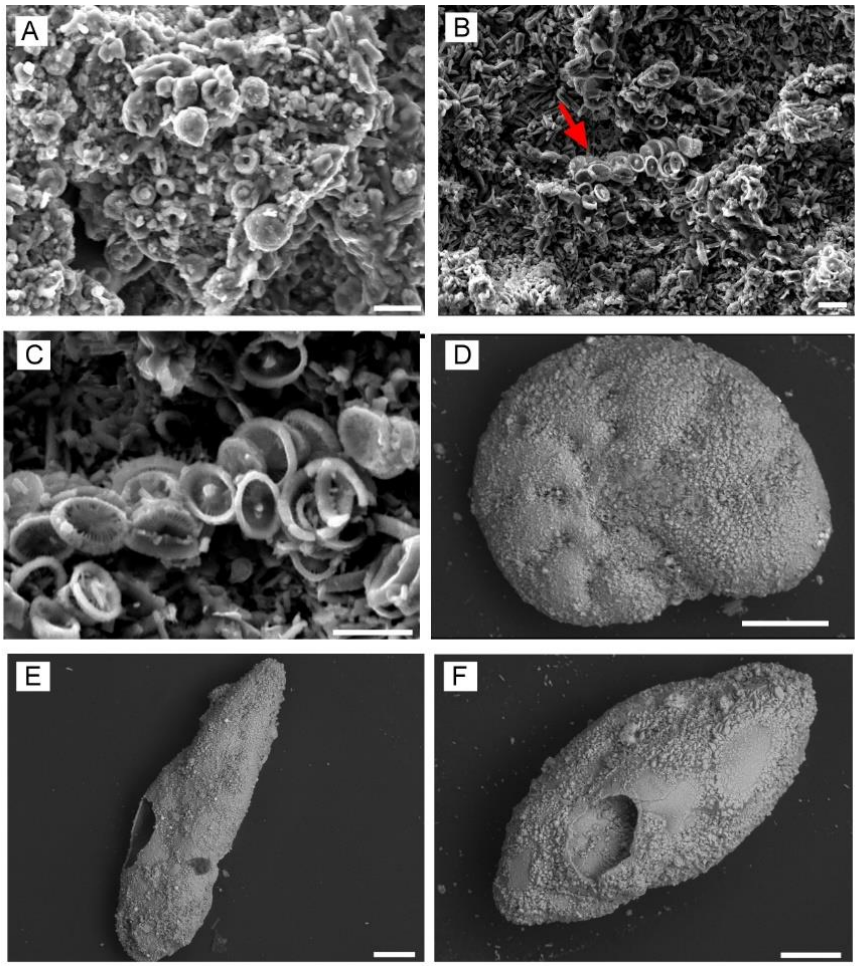

Fig. 4: SEM images of freshly broken sediment surface and hand-picked foraminifers from the Los Molinos samples. A: Fecal pellet mostly composed by CN (cycle PLG4). B: Disrupted coccosphere of *Syracosphaera pulchra* (red arrow) in an aragonitic matrix (cycle PLG7). C: close up of B; with a cluster of coccoliths of *Syracosphaera pulchra* showing dissolution and fracturing features. D: Benthic foraminifer showing calcite encrustation (cycle PLG7); oxidised pyrite is also present as a minor component of the encrustation E: Encrusted and fragmented *F. fusiformis* (cycle PLG6). F: A miliolid showing dissolution of the external wall and calcitic/pyritic encrustations (cycle PLG7).

4.4 C and O stable isotope analyses

The stable isotope results were plotted and compared with the stable isotope composition of the Great Bahamas Bank aragonite and with biological sourced aragonite (i.e. codiacean algae, *Halimeda* and skeletal material; Fig. 8). The aragonite laminae show positive $\delta^{13}C$ values ranging from +2.49 to +3.56 ‰ whereas the $\delta^{18}O$ values are slightly negative (from -2.28 to -0.25 ‰) (Fig. 8). The $\delta^{13}C$ and $\delta^{18}O$ values of the limestone layers belonging to cycles PLG6, PLG7, PLG9 and PLG11 fluctuate from -1.09 to +1.04 ‰ and from -4.75 to +4.73 ‰, respectively (Fig. 8). The lowest $\delta^{18}O_{limestone}$ values were recorded in cycles PLG9 and PLG11 (-3.73 and -4.75 ‰, respectively; Fig. 8), while limestones from cycles PLG6 and PLG7 showed higher values (+4.73 and -0.36 ‰, respectively).

5 Discussion

5.1 The influence of taphonomic processes on the distribution of calcareous micro and nannofossils.

The influence of taphonomic processes on the distribution of calcareous micro and nannofossils in the different intervals of the studied succession is discussed herein based on the whole micropaleontological, petrographical and isotopic dataset.

5.1.1 The pre-MSC/MSC transition

Several evidences suggest an upward increase of calcite dissolution starting from the base of cycle UA34:

a) the increase of the relative abundance of dissolution-resistant CN taxa (i.e. *C. pelagicus* and *R. pseudoumbilicus*; supplementary material Fig. 4) toward the MSC onset and the complete disappearance of CN in the second limestone layer of cycle UA34 (Fig. 5). *Coccolithus pelagicus* and *R. pseudoumbilicus* are among the most dissolution-resistant taxa (Roth and Berger, 1975; Roth and Coulbourn, 1982; Gibbs et al., 2004), thus their dominance, together with the absence of dissolution-prone CN specimens, suggests that the observed CN assemblage was likely influenced by dissolution of biogenic calcite.

b) The deterioration of the preservation quality of the calcareous microfossils with respect to the underlying cycles (Fig. 4, A4 and $A4_2$; supplementary material Fig. 2; Fig. 3).

c) The order of micro and nannofossil disappearance (PF, CN and finally BF) is fully consistent with laboratory and sediment trap observations showing that PF are more susceptible to dissolution than CN and BF (Peterson and Prell, 1985; Steinsund and Hald, 1994; Chiu and Broeker, 2008; Subhas et al., 2018). Our observations are therefore consistent with the notion that biogenic calcite in in the analysed samples was progressively dissolved.

d) The absence of reworked specimens of calcareous fossils, that is in contrast with the evidence of sediment reworking at the MSC onset (e.g. Natalicchio et al., 2019; Sabino et al., 2020).

e) The presence of internal moulds of foraminifers filled with pyrite or oxidised pyrite (Fig. 5 A3, $A3_2$) in the layers recording the PF and BF disappearance in the washing residue. The dissolution of the calcitic wall of foraminifers led to the formation of empty cavities between the pyrite infill and the surrounding sediment (Fig. 5, A3). These features indicate that the foraminifer disappearance was related to the dissolution of the test, which likely occurred during early diagenetic phases in the taphonomically active zone. SEM observations show that the content in pyrite foraminifer moulds increases upwards, peaking in the second limestone layer of cycle UA34 (Fig. 4 B1 and $B1_2$; supplementary material Fig. 5) where no calcareous microfossils were observed in washing residues

and smear slides. Indeed, standard micropaleontological methods (i.e. disaggregation, treatment with peroxide and the successive sieving of the sediment) result in the alteration of delicate sediment components such as pyrite moulds, that can be unnoticed with optical microscope investigations of the washing residues and smear slides.

f) The total absence of carbonate grains in the blue clay level above the second limestone layer of cycle UA34, suggesting the exacerbation of dissolution processes just below the first PLG cycle (Fig. 2).

g) Pyrite aggregates mimicking BF shape were observed in the marly hemicycles of cycles PLG1 and PLG2, suggesting intense carbonate dissolution also in these intervals (Fig. 5, B3)

The presence of oxidised pyrite moulds after foraminifers may reflects the degradation of organic matter (i.e. foraminifer cytoplasm) through bacterial sulphate reduction in an anoxic microenvironment, which took place within the foraminifer test either in the water column or at the sea floor (Buckman et al., 2020) following the reactions:

(1) $2CH_2O + SO_4^{2-} \rightarrow H_2S + 2HCO_3^-$

(2) $Fe^{2+} + H_2S \rightarrow FeS_2 + H_2$.

Subsequent pyrite oxidation, according to the reaction:

(3) $FeS_2 + 7/2O_2 + H_2O \rightarrow Fe^{2+} + 2SO_4^{2-} + 2H^+$.

Pyrite oxidation increases local acidity which could trigger dissolution of biogenic calcite (McNeil, 1997; Buzas-Stephens and Buzas, 2005; Liu et al., 2018) as observed in our material. Small sized pyrite (<10 µm) was also consistently found in this interval, suggesting euxinic condition in the lower water column (Bond and Wignall, 2010; Tagliavento et al., 2020).

Dissolution of biogenic calcite could also take place in aerobic conditions through the degradation of organic matter, according to the reaction:

(4) $CH_2O + O_2 \rightarrow CO_2 + H_2O$.

The production of CO_2 increases acidity, in turn promoting dissolution of biogenic calcite (Archer and Maier-Reimer, 1994; Jahnke et al., 1997; Archer, 2003; Suárez-Ibarra et al., 2022) according to the reaction:

(5) $CO_2 + CaCO_3 + H_2O + \leftrightarrow 2HCO_3^- + Ca^{2+}$.

Based on these evidences, we suggest that the disappearance of biogenic calcite reflects a taphonomic bias, related to the accumulation and the subsequent oxidation of pyrite and organic matter at the sea floor.

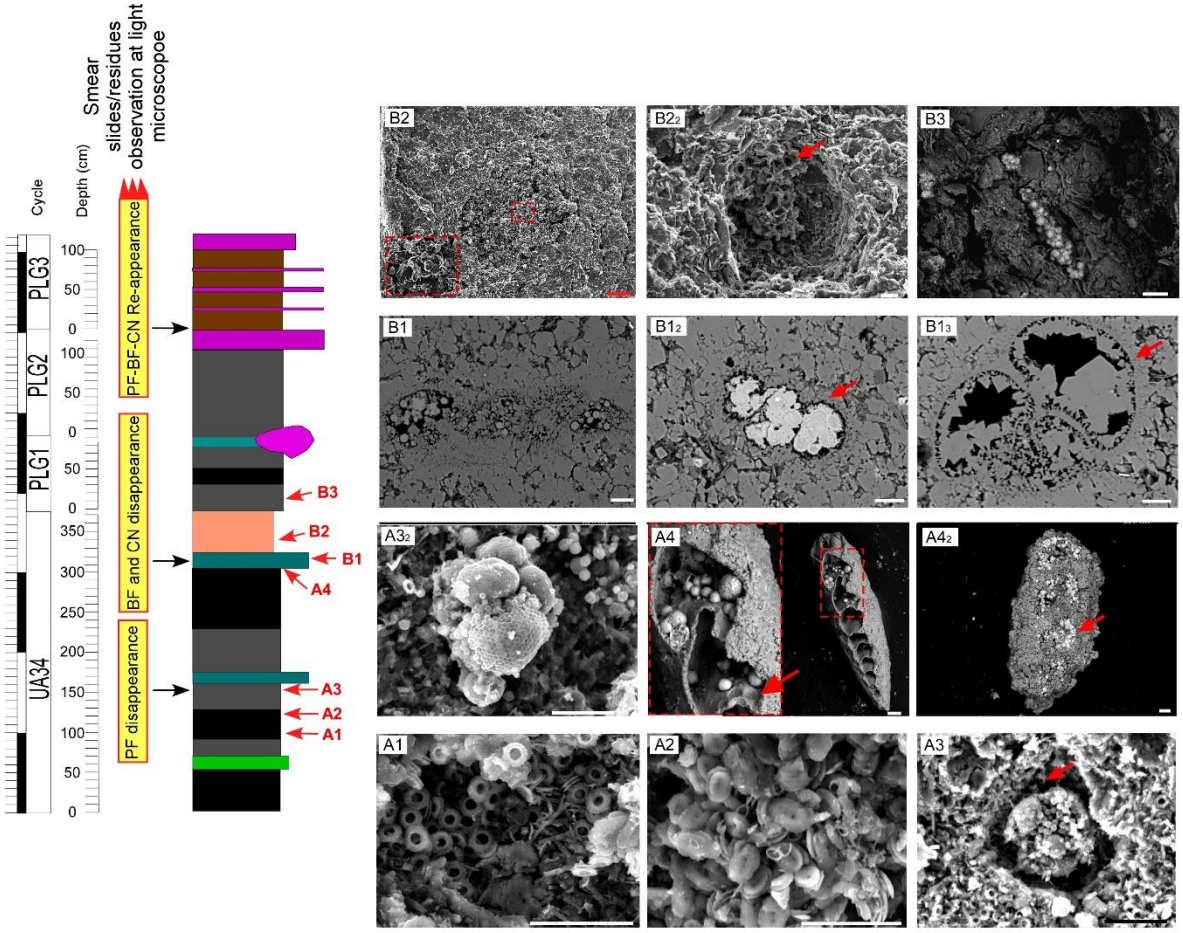

Fig. 5: Left: stratigraphic column of the interval encompassing the MSC onset in the Perales section with location of the samples recording the disappearance of the micro and nannofossils as observed in the washing residues and smear slides. On the right, SEM images from stubs or thin sections and from handpicked foraminifers. The red numbered letters in the stratigraphic section indicate the location of the samples. Gypsum layers of cycles PLG 2 and PLG3 are not to scale. A1: High abundance of *U. rotula* characterizing the MSC onset bioevent. A2: High abundance of *H. carteri* characterizing the MSC onset bioevent. A3: Putative pyrite mould after foraminifer. The red arrow indicates the empty space (previously occupied by the test) between the pyrite and the sedimentary matrix. $A3_2$: Putative pyrite internal mould after a dwarf foraminifer test, probably a Turborotalid. A4: Hand-picked benthic foraminifer belonging to the genus *Bolivina*. The specimen shows dissolution feature on the shell margin. Red arrows indicate oxidised pyrite that leaves dissolution pits on the internal calcitic wall. $A4_2$: Handpicked benthic foraminifers showing large calcitic encrustation and oxidised pyrite infills. Red arrow shows the boundary between the oxidised pyrite and the calcitic wall, the latter is partially dissolved. B1: Back scattered SEM images of polished thin section showing a dissolved phosphatic fish remain with oxidised pyrite infills. $B1_2$: Back scattered SEM images of polished thin section showing a putative pyrite mould after a foraminifer. Red arrow shows the replacement of the original calcitic wall with fine grained calcite. $B1_3$: Back scattered images of polished thin section showing a foraminifer with large calcitic crystals close to the wall. Red arrow indicates the highly altered foraminifer wall. B2: SEM image of freshly broken sediment surface of the blue/grey clay interval, showing a rounded cavity filled with quartz crystals and surrounded by a siliciclastic matrix. The carbonate component of this layer is nearly absent (supplementary material Fig. 6). $B2_2$: Void with oxidised pyrite with honeycomb structure. B3: Oxidised pyrite mimicking a dwarf benthic foraminifer. Scale bar is 20 µm, except in B2, in which is 100 µm

5.1.2 The PLG unit

Rare to common foraminifers and CN are discontinuously present from cycle PLG3 upward (i.e. 5.93 Ma onward), still showing dissolution evidence and a variable degree of preservation (Fig. 4; supplementary material Fig. 8). On the other hand, the content of organic matter and oxidised pyrite

in the sedimentary matrix and in the foraminifer chambers is significantly lower compared to the underlying sediments. Such observation agrees with the notion that the preservation of biogenic calcite is tightly linked with oxidation of pyrite and of organic matter (see paragraph 5.1.1).

Aragonite laminae were observed in the marly hemicycle of cycles PLG4 and PLG7. The aragonite/calcite stability is mostly controlled by the Mg/Ca ratio in sea water (Morse et al., 1997; Bots et al., 2011). In particular, if Mg/Ca > ~ 0.6–0.7, aragonite becomes the dominant phase, and with values of ~1.7 only aragonite precipitates. The Mg/Ca ratio and the temperature control the substitution of Mg^{2+} in the calcite lattice (Burton and Walker, 1991), which ultimately drives the thermodynamic stability of calcite. In addition, Bots et al. (2011) showed that an increase in dissolved SO_4^{2-} decreases the Mg/Ca ratio at which calcite is destabilized and aragonite becomes the dominant $CaCO_3$ polymorph. We thus suggest that the presence of well-preserved aragonite and the contextual poorly preserved biogenic calcite in cycles PLG4 and PLG7 may reflect an increase in dissolved Mg^{2+} and SO_4^{2-} ions in the water column. This mechanism could represent an additional cause for the poor preservation of micro and nannofossils in the PLG unit.

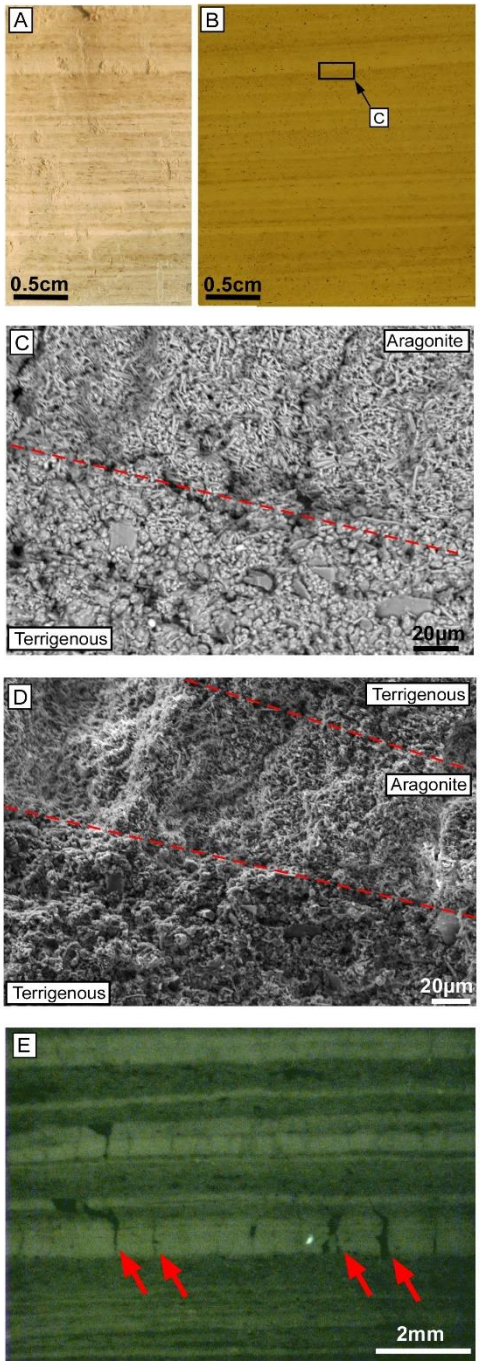

Fig. 6: The laminated marls from cycles PLG4 and PLG7. A: Polished slab of a freshly broken sediment chip. B: Photomicrograph (transmitted light) of the same sample as in A; the black square shows the position of C. C: SEM image (polished thin section) showing the alternation of the terrigenous and the aragonitic laminae. Note the longitudinal cracks in the aragonitic lamina; red dotted line defines the boundary between the laminae. D: SEM image of freshly broken sediment showing the alternation of the terrigenous lamina and the aragonitic lamina; red dotted line defines the boundary between the lamina. E: UV light photomicrograph of laminated sediment; note the bright autofluorescence of the aragonite laminae and the vertical cracks (red arrows).

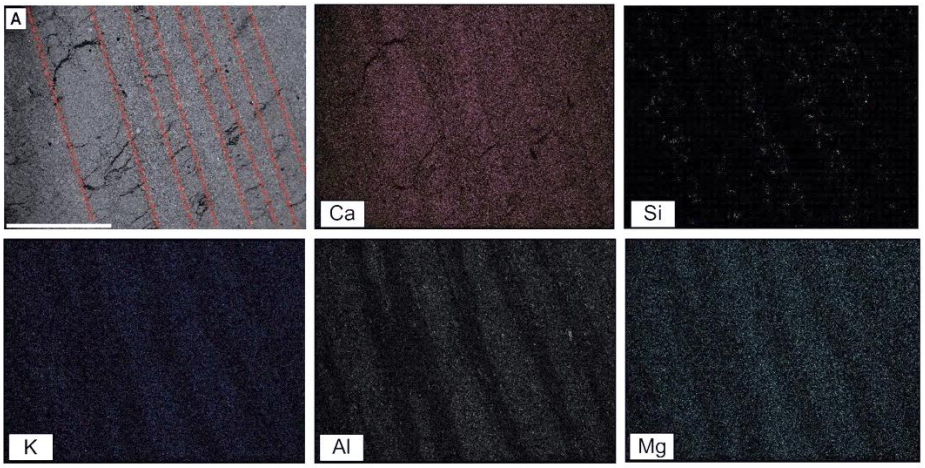

Fig. 7: Representative SEM images and elemental maps (Ca, Si, K, Al and Mg) of the laminated marls from cycles PLG4 and PLG7 (polished thin sections). A is the reference image; the red dashed lines indicate the lower and upper boundaries of the aragonite laminae.

5.2 Paleoenvironmental condition leading to the dissolution of calcareous tests

There are consistent evidences that the micro and nannofossil records of the uppermost pre-evaporitic phase (cycle UA34) and of the PLG unit are biased by dissolution of calcareous tests resulting from pyrite and organic matter oxidation and changes in Mg^{2+} and SO_4^{2-} content in seawater. These processes were triggered by paleoenvironmental changes as recorded by sedimentological, petrographical and micropaleontological data. Indeed, just prior to the MSC onset, cycle UA34 records an exceptional and prolonged increase of organic matter preservation (Fig. 2) during both insolation maximum (wetter and warmer conditions) and minimum (drier and colder conditions), marking a striking difference with respect to the older UA cycles, where grey homogeneous marls and diatomites are intercalated between organic rich layers (Sierro et al., 2001). Apparently, in UA34, warmer/wetter and drier/colder phases are recorded by the alternation of intervals characterized by prevalent laminated or weakly laminated sediments, respectively (Fig. 2). This alternation created the condition for pyrite formation and organic matter accumulation during phases of bottom anoxia and water column stratification (warmer/wetter periods), and their subsequent oxidation during more mixed conditions (drier/colder periods). Since the same climatic alternations are involved in the "normal" UA cyclicity at the precessional scale (Sierro et al., 2003; Mancini et al., 2020) without any strong evidence of dissolution of biogenic calcite, it is reasonable to hypothesize that the final restriction of the basin (cycle UA34, just below the MSC onset) favoured calcite dissolution by increasing the sensitivity to external (climatic) forcing, such as (seasonal) variation in the freshwater input and temperature, which promoted fluctuations of bottom redox conditions.

During the pre-evaporitic phase, several lines of evidence suggest a gradual progression towards more restricted conditions (Kouwenhoven et al., 2006; Vasiliev et al., 2019; Kontakiotis et al., 2019; Corbí et al., 2020; Zachariasse et al., 2021; Bulian et al., 2022; Kontakiotis et al., 2022). Indeed, a Mediterranean scale restriction step increased organic matter accumulation at every

insolation maximum from 6.7 Ma (Sierro et al., 2001; Sierro et al., 2003; Mayser et al., 2017; Kontakiotis et al., 2020; Kontakiotis et al., 2021). Similarly, toward the MSC onset increasing runoff influence is suggested by the oxygen stable isotope composition of foraminifer tests from ~6.1 ($\delta^{18}O_{neogloboquadrinids}$ down to -4‰; Reghizzi et al., 2017). A freshening of the water column was recorded also in the Eastern Mediterranean at the same time (Vasiliev et al., 2019). Finally, in cycle UA34, the abundance peaks of *S. abies* and *H. carteri* (part of the MSC onset bioevent), both able to thrive in freshwater-influenced environments (see Mancini et al., 2020), and the lithological changes described above suggest enhanced influence of river runoff, promoting surface water freshening, nutrient input, water column stratification and high productivity (Mancini et al., 2021). We infer that marked climate-induced fluctuation of oxygen content at the bottom took place, promoting pyrite formation and organic matter preservation during anoxic phases (wet/warm season; Fig. 9A), and their successive oxidation during oxygenated phases (arid/cold season; Fig. 9B). These mechanisms, involving a marked fluctuating oxycline, likely led to the progressive dissolution of foraminifers and CN toward the MSC onset (Fig. 9A and Fig. 9B). Carbonate dissolution reached the acme in the blue clay level (Fig. 2), that is almost devoid of carbonate grains (supplementary material Fig. 6). Although the lack of carbonate grains should be investigated with greater detail, the concomitant absence of reworked calcareous taxa suggests that such a pattern is not the result of a biocalcification reduction, as previously suggested (Blanc-Valleron et al., 2002; Rouchy and Caruso, 2006). At the beginning of the MSC, sediments of cycles PLG1 and PLG2 still yield pyrite moulds, but their link with BF is not straightforward. Thus, the absence of calcareous microfossils in washing residues and smear slides cannot be unambiguously interpreted in terms of a taphonomic bias. However, marine fossils (fishes, echinoids, bivalves, bryozoans and gastropods) were recorded in coeval shallower sediments from the Sorbas Basin (Los Yesos section, Montenat et al., 1980; Saint Martin et al., 2001; Goubert et al., 2001; Néraudeau et al., 2002) and neighbouring basins (Carboneras-Nijar Basin, Van de Poel, 1992). Indeed, in the more marginal and shallow part of these basins (i.e. Los Yesos), the mixed layer delivering oxygen could have reached the sea bottom, hampering pyrite and organic matter accumulation. From cycle PLG3 upward, decreased pyrite and organic matter accumulation was possibly responsible for improved preservation of calcareous micro and nannofossils which, however, still show dissolution evidence (Fig. 3, Fig. 4; supplementary material Fig. 8). The presence of aragonite in some cycles and the poor preservation of calcite fossils could reflect an increase of dissolved Mg^{2+} and SO_4^{2-} ions in seawater (paragraph 5.1.2). Although additional investigations are needed to constrain the sources of Mg^{2+} and SO_4^{2-} , the CN assemblage (for more detail, see 5.4 paragraph) supports the hypothesis that the SO_4^{2-} and the Mg^{2+} were river-delivered, since taxa such as *H. carteri*, *Sphenolithus* gr. and *C. pelagicus*, adapted to low salinity conditions (Giraudeau et al., 1992; Silva et al., 2008; Auer et al., 2014; Mancini et al., 2020) are common in these layers (Fig. 3). In particular, among these taxa, *C. pelagicus* was observed to thrive at salinity down to 26.5 ‰ (Silva

et al., 2008).

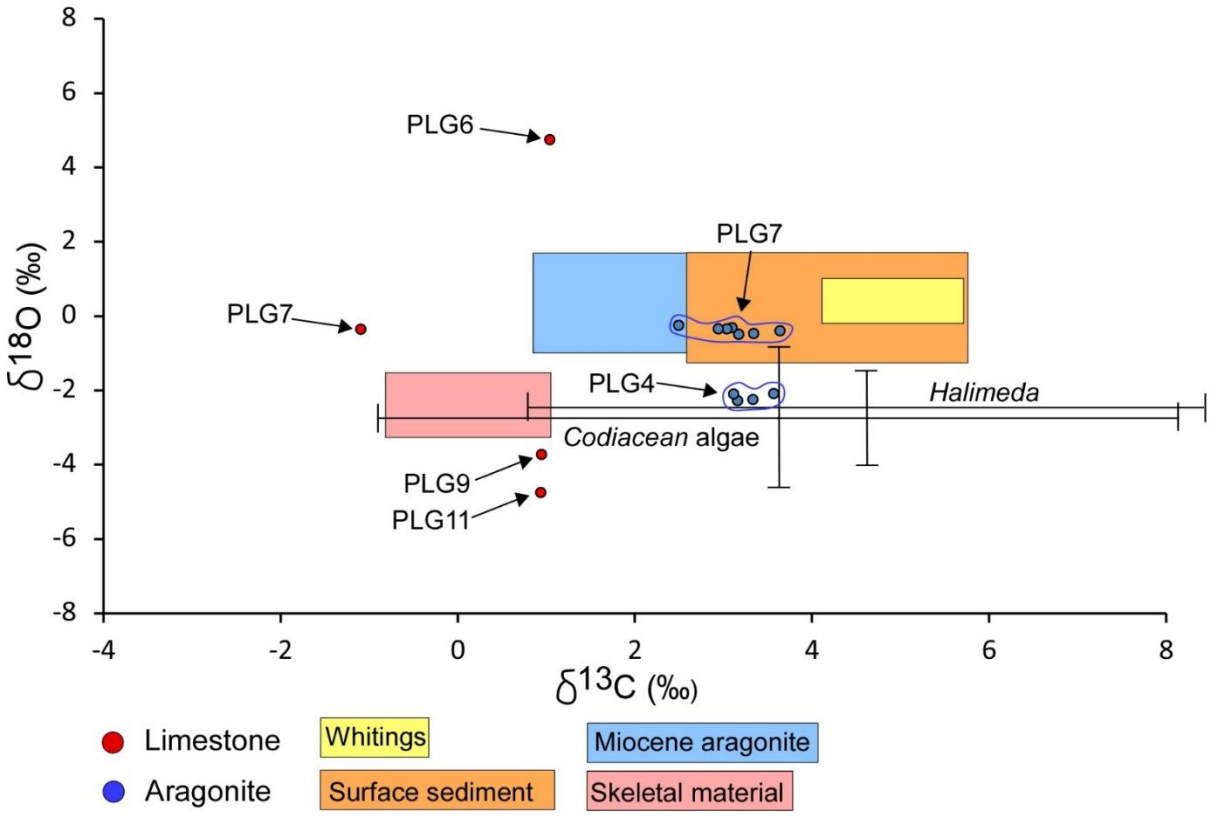

Fig. 8: Oxygen and Carbon stable isotope composition of aragonite laminae and limestone layers belonging to the PLG unit. Data are compared with the stable isotope composition of aragonite from the Great Bahamas Bank. Data from Shinn et al., 1989 (yellow rectangle; suspended materials); Swart et al., 2009 (orange rectangle, surface sediment); Turpin et al., 2011 (light blue rectangle; Miocene); Weber, 1966; Milliman, 1974; Swart, 1983 (pink rectangle; skeletal materials of scleractinian corals and echinoids); Lee and Carpenter, 2001 (*Halimeda* and Codiacean algae; black lines).

5.3 The aragonite and its paleoenvironmental significance

The aragonite crystals found in the laminated deposits of the marly hemicycles of cycles PLG4 and PLG7 display shape and size similar to the Bahamas aragonite (Loreau, 1982, page 39 Fig. d; Shinn et al., 1989, Fig. 9 a, b, c and d; MacIntyre and Reid, 1992, Fig. 1 a and b; Milliman et al., 1993, Fig. 2 a, b and c). The slightly negative $\delta^{18}O$ values (from -2.28 to -0.25 ‰) of the studied aragonitic laminae suggest that aragonite did not precipitate from evaporated sea water; in this case, positive values (up to 9‰) should be expected (Ziegenbalg et al., 2010). Aragonite is ^{13}C-enriched ($\delta^{13}C$ values from +2.49 to +3.56 ‰) compared to the present-day Mediterranean surface water ($\delta^{13}C$ +0.96 to +1.52 ‰; Pierre, 1999) and Tortonian bulk calcite from Lorca Basin, SE Spain ($\delta^{13}C$ -1.8 to +0.2 ‰ Pierre and Rouchy, 2004). Such ^{13}C enrichment may reflect intense photosynthetic activity in the upper water column; indeed, photosynthesis preferentially removes ^{12}C causing the water to become enriched in the heavier ^{13}C isotope (Robbins and Blackwelder, 1992; Swart and Eberli, 2005; Swart et al., 2009). Therefore, we suggest that aragonite precipitation in the water column of the Sorbas Basin could have been induced by autotroph blooms (Robbins and Blackwelder, 1992; Obst et al., 2009;

572 Swart et al., 2009;; Sondi and Juračić, 2010) which decreased the local pCO_2 and increased alkalinity,
573 favouring the precipitation of carbonate minerals (calcite and aragonite) (Larson and Mylroie, 2014).
574 Aragonite-rich deposits were observed across the MSC onset and during the first MSC phase in Sicily
575 (Italy), but their different isotopic signature ($\delta^{13}C$ values from -49 to -36 ‰ and $\delta^{18}O$ values from +5
576 to +5.6 ‰, Zieglenblag et al., 2010; $\delta^{13}C$ from -1 to +1.9 ‰ and $\delta^{18}O$ from +3 to +7.4 ‰, Perri et al.,
577 2017) with respect to the crystals studied here, suggests a different origin. On the other hand, the
578 isotopic signature of the Sorbas Basin aragonite is similar to that of Middle Miocene and modern
579 sediment of the Great Bahamas Bank (Fig. 8; Shinn et al., 1989; Turpin et al., 2011). Therefore, we
580 suggest that possible analogues of the Sorbas Basin aragonite are the so-called "whiting" of the Great
581 Bahamas Bank (Robbins and Blackwelder, 1992; Swart et al., 2009). Localised aragonite precipitation
582 can also take place within extracellular polymeric substance (i.e. EPS) (Obst et al., 2009) produced by
583 picoplankton, phytoplankton and green algae (Yates and Robbins, 1998). In modern environments,
584 aragonite can be also biogenically produced by algae (e.g. *Halimeda*), with isotopic signature in the
585 range of our results (Fig. 8), but the habit of the resulting crystals differs from that of the crystals
586 deriving from whitings (Lorau, 1982; MacIntyre and Reid, 1992; Shinn et al., 1989; MacIntyre and
587 Reid, 1995). Aragonite microcrystals from *Halimeda* are 3 to 10 μm long and show sharp-faced
588 crystals and blunt terminations; in addition, the majority of crystals produced by *Halimeda* are in the
589 form of nanograins (≃ 1 μm; MacIntyre and Reid, 1992). Despite *Halimeda is* widely reported in
590 carbonate platform deposits surrounding the Sorbas Basin at the time of PLG deposition (Roveri et al.,
591 2009; Roveri et al., 2020), the habit of the studied aragonite crystals is not consistent with this source.

592 The bio-mediated origin of aragonite is further supported by:

593 1- The bright auto fluorescence (Fig. 6E) of the aragonite laminae, reflecting high contents of
594 organic matter, possibly associated with autotrophic activity during intense bloom episodes.

595 2- The longitudinal cracks within the aragonite laminae, which may result from degradation of
596 EPS, acting as a template for aragonite nucleation (Obst et al., 2009).

597 We thus suggest that precipitation of aragonite in the PLG unit was biologically-mediated by
598 unknown phototrophs organisms. Possible candidates are not-fossilizing cyanobacteria or siliceous
599 algae. The concomitant presence of aragonite precipitated in the upper water column and small size
600 pyrite, indicative of euxinic condition in the lower water column (Bond and Wignall, 2010;
601 Tagliavento et al., 2020), suggests the vertical separation of the water column by an oxycline (Fig.
602 10).

603

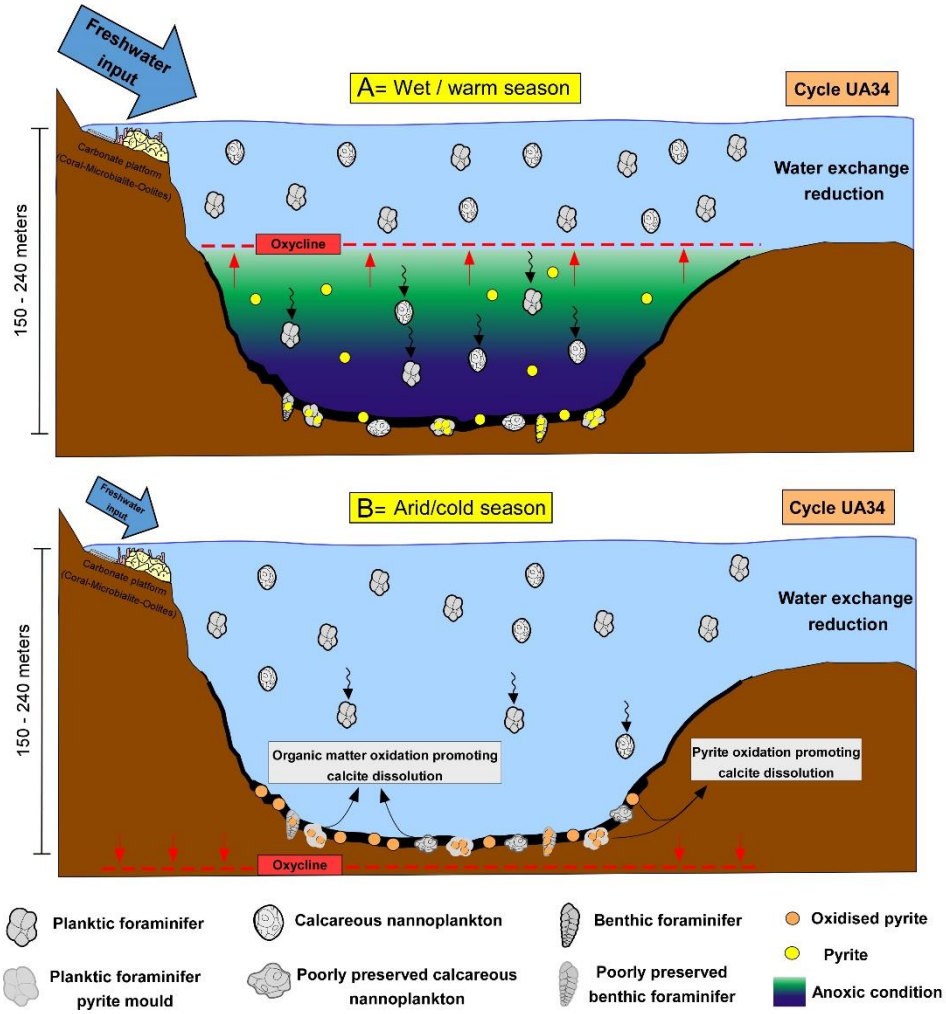

Fig. 9: Sketches showing the mechanisms promoting dissolution of calcareous fossils. A: During the wet/warm season, enhanced freshwater input caused density stratification of the water mass. Sinking organic matter and its consequent remineralisation promoted sea bottom anoxia and the establishment of an oxycline separating oxygenated surface water and anoxic/euxinic bottom water. Below the oxycline, pyrite precipitated and sunk to the bottom. Pyrite was also formed inside foraminifer shells. B: During the arid/cold season, sea water cooling and reduced freshwater input caused the vigorous mixing of the water column, with consequent migration of the oxycline below the seafloor. This mechanism promoted the oxidation of both organic matter and pyrite, which ultimately triggered the dissolution of the biogenic calcite.

5.4 The micro and nannofossil assemblage in the PLG unit and its paleoenvironmental meaning

Calcareous micro and nannofossils re-appear in the washing residues and smear slides from cycle PLG3 upward (5.93 Ma) where they are discontinuously present, showing variable preservation (Fig. 3 and Fig. 5; supplementary material Fig. 8). Overall, little paleoenvironmental information can be obtained by the micro and nannofossil assemblage recorded in the PLG unit, because the composition of the assemblage is controlled by preservation. However, the presence of intact coccospheres and the low abundance of reworked CN in these cycles (Fig. 3) is an indication that, where preserved, the calcareous microfossil assemblages are synsedimentary and not reworked.

The appearance of shallow water ostracods (i.e. *Cyprideis*) from cycle PLG4 upwards indicates an overall shallowing of the basin with respect to the pre-MSC cycles. In the middle part of the marly hemicycle of cycle PLG6, *F. fusiformis* specimens are common, though often fragmented.

Fursenkoina fusiformis is an opportunistic shallow infaunal species (inner shelf zone) associated to high organic carbon input to the sea floor, even though it can be sensitive to oxygen depletion (Barmawidjaja et al., 1992; Alve and Murray, 1994). In the Northern Indian Ocean, high percentages of this genus are associated to the shallow portion (50-60 m) of the Oxygen Minimum Zone (Mazumder and Nigam, 2014) and it was also found at less than 40 m in the North Adriatic Sea in front of the Po delta (Barmawidjaja et al. 1992). Among its ecological preferences, it is worth noting the ability to rapidly recolonise the shelf after anoxic events (Alve and Murray, 1994).

Upward in the section, in cycle PLG7, BF are less frequent and often mostly present in the < 125 µm (Fig. 3). The assemblage composition (bolivinids, buliminids, uvigerinids and *Globobulimina*) also suggests high organic carbon rain to the sea floor. The shallowing upward trend is further confirmed by the rather common occurrence of miliolids (*Quinqueloculina* sp.) in the marly hemicycle of cycle PLG9 (Fig. 3). *Quinqueloculina* is an epifaunal taxon often associated with hypersaline lagoons, marine marshes or inner shelf settings (Murray, 2006); together with the presence of *Cyprideis* species it suggests euryhaline conditions and the decline of organic matter availability at the seafloor with respect to the lower PLG cycles. Previous studies indicated a paleodepth spanning from 150-240 meters at the Abad/Yesares transition (Dronkert, 1976; Troelstra et al., 1980; van de Poel, 1992; Riding et al., 1998; Baggley, 2000; Clauzon et al., 2015; Modestou et al., 2017), and to 75-100 meters at the Yesares/Sorbas transition (Krijgsman et al., 2001; Roveri et al., 2020), which is consistent with our data. However, the presence of miliolids, *Ammonia*, *Elphidium*, and *Cyprideis*, suggests a shallower water body (less than 75 m), probably a lagoon characterized by salinity fluctuations (see also Van de Poel, 1992).

Cycles PLG11 and PLG 12 are prevalently barren of microfossils, except for the uppermost sample of cycle PLG11, where *Ammonia*, *Elphidium* and miliolids are present, confirming shallow environmental conditions and salinity fluctuations (Murray, 2006).

The presence of calcareous plankton in such shallow environment has been often considered as the result of reworking. However, in modern settings, calcareous nannoplankton (i.e. Coccolithophores) was reported to proliferate in shallow (even less than 30 m) lagoonal environments (Sakka et al., 1999; Sondi and Juračić, 2010; Dimiza et al., 2020), where it could be adapted to low salinity conditions (Paasche et al., 1996). In modern settings, coccolithophores are recorded in low salinity environments, where they can even massively bloom, as in the case of the Black Sea (Sea surface Salinity ~ 18 ‰; Tyrrel et al., 2008; Kubryakov et al., 2021). They were recorded also in the Baltic Sea (Kieler Forde, where maximum coccolithophore abundance occurred at salinity of 18 ‰; Meier et al., 2014) and in the Aegean Sea (Thessaloniki bay, where coccolithophore maximum abundance is reached with salinity of 17 ‰; Dimizia et al., 2020).

In our case, the CN assemblage consists of taxa tolerating low salinity conditions, such as *H. carteri*, *Sphenolithus* gr. and *C. pelagicus* (Giraudeau et al., 1992; Silva et al., 2008; Auer et al., 2014;

Mancini et al., 2020), especially in cycles PLG6, PLG7 and PLG11 (Fig. 3). The scarce occurrence of PF in the PLG unit could be related to the reduced water depth in respect to the pre-evaporitic phase, because PF often require > 75 m water column (Schiebel and Hemleben, 2017). Furthermore, the low salinity condition characterizing surface waters during the marly PLG hemicycle deposition could have prevented the proliferation of PF, similarly to what observed in the modern Black Sea, where living PF were never reported (Aksu et al., 2002; Gavrilova and Dolan, 2007; Wylezich and Jürgens, 2011). Therefore, the scattered occurrence of open marine PF (i.e *T. quinqueloba* and *Globigerinoides*; Fig. 3) could suggest episodic improvement of the connection with the open sea (Fig. 11).

The shallowing of the Sorbas Basin from cycle PLG 3 (5.93 Ma) led to salinity fluctuations in a restricted environment influenced by freshwater inflows and evaporation. Runoff could have led to the formation of a pycnocline; however, anoxic bottom conditions were only occasionally established, as denoted by the scattered presence of pyrite and organic matter.

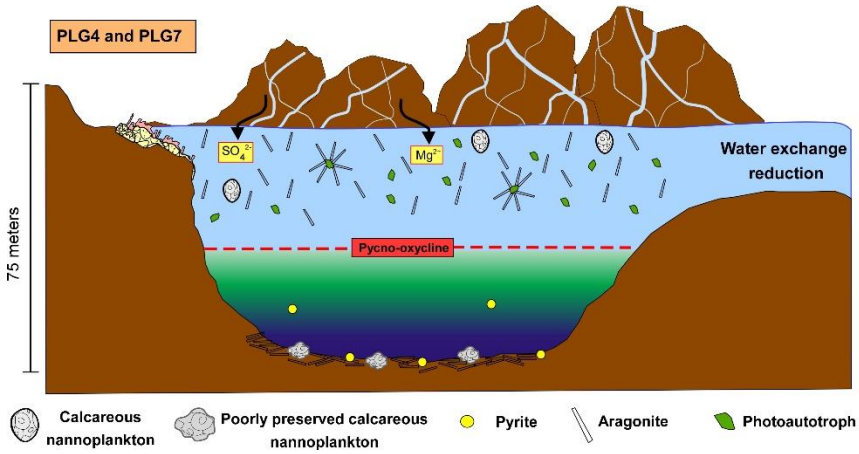

Fig. 10: Sketch showing the inferred mechanisms that promoted aragonite deposition and concomitant dissolution of biogenic calcite in the PLG unit. Ongoing basin restriction resulted in an increased concentration of river-delivered Mg^{2+} and SO_4^{2-} ions, favouring precipitation of bio-mediated aragonite and dissolution of biogenic calcite.

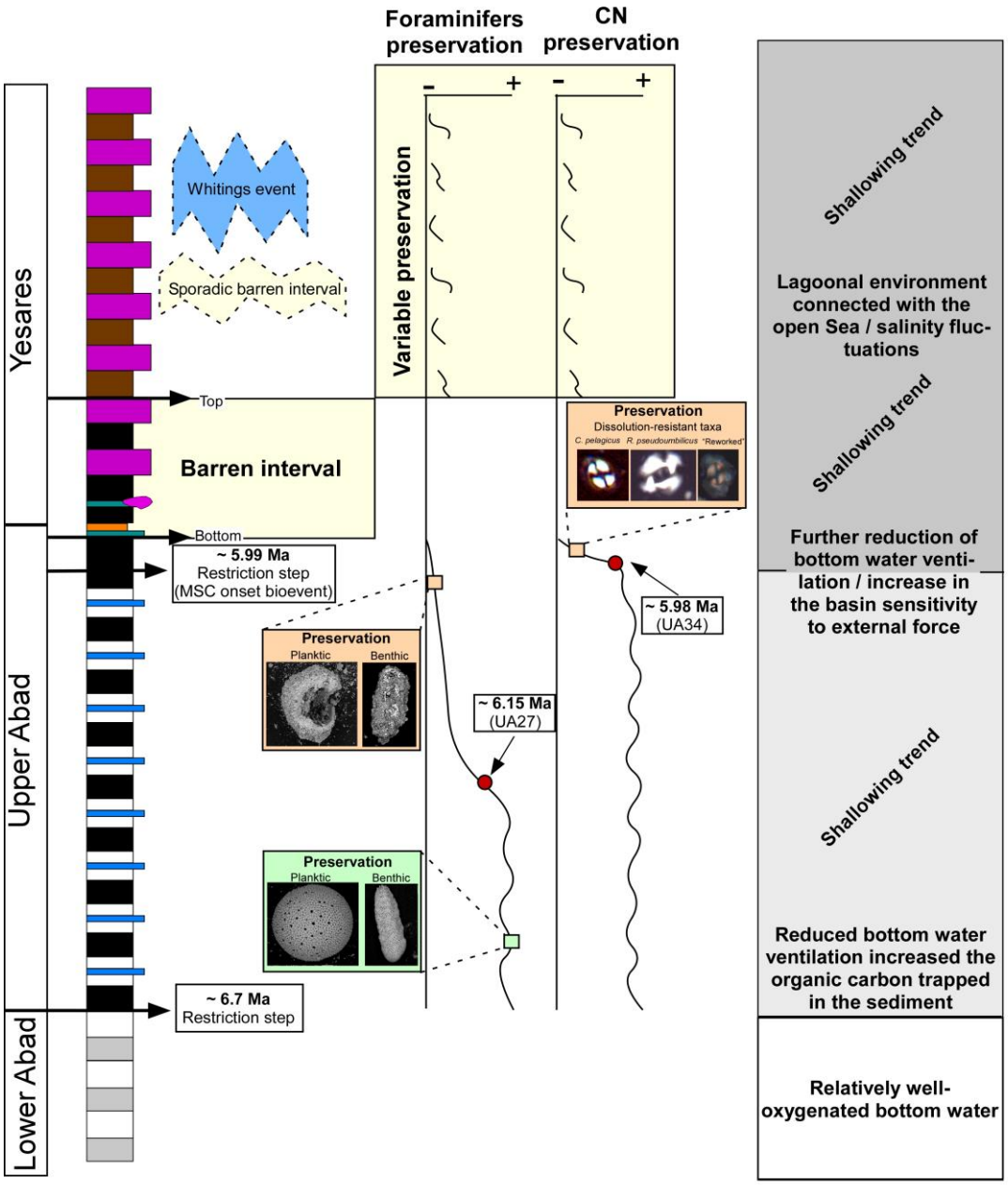

Fig. 11: The paleoenvironmental evolution of the Sorbas Basin toward the onset and during the MSC, with the main taphonomic features characterizing the micro and nannofossil assemblage. The number and the thickness of the lithological cycles are schematic. Red dots indicate the beginning of the deterioration in the preservation of calcareous micro and nannofossils. Green square indicates relatively good preservation; orange squares indicate relatively bad preservation.

Conclusion

The micropaleontological, mineralogical, sedimentological and isotopic characterization of the sediments spanning the onset and the first phase of MSC from the Sorbas Basin suggests that paleoenvironmental changes in the uppermost pre-evaporitic interval (i.e. cycle UA34) led to

dissolution of biogenic calcite. In this interval, no evidence of increased salinity was found; rather the high content of *S. abies* and *H. carteri* that characterizes the MSC onset bioevent suggests the freshening of the upper water column. Calcite dissolution and the consequent disappearance of calcareous micro and nannofossils approaching the MSC onset was triggered by pyrite and organic matter oxidation, following climate-induced fluctuations of the redox conditions in the bottom waters of a restricted basin. The calcitic fossils reappeared from 5.93 Ma onward (cycle PLG3), but the assemblages are usually poorly preserved and quantitatively scarce; this fossil content is mostly synsedimentary (i.e. not reworked) and still indicates restricted conditions, but in a progressively shallower basin, less prone to fluctuations of redox conditions in the bottom water. The precipitation of aragonite, in cycles PLG4 and PLG7, was likely bio-mediated through bloom of not-fossilising autotroph organisms. Aragonite stability was likely favoured by an increase in (river-delivered) Mg^{2+} and SO_4^{2-} in the seawater, which was also responsible for the poor preservation of calcitic fossils. The scattered occurrence and low abundance of the open marine taxa also reflects unstable conditions in a confined (lagoon) environment.

Our results indicate that the micropaleontological record at the onset and during the first phase of the MSC (PLG unit) is strongly biased by dissolution of calcitic micro and nannofossils; such taphonomic bias must be considered in the paleonvironmental reconstructions of the MSC events and in the use of the disappearance of calcareous microfossil as a biostratigraphic marker approximating the onset of the MSC.

Acknowledgment

We thank S. Cavagna for the assistance during SEM investigation, G. Della Porta for the assistance with the isotope analysis and to F. J. Sierro and F. J. Hilgen for the discussions and suggestions emerged during the field trip in Sorbas. We thank two anonymous Reviewers and H. Corbí for their comments and suggestions which improved the quality of the manuscript.

References

Aksu, A. E., Hiscott, R. N., Kaminski, M. A., Mudie, P. J., Gillespie, H., Abrajano, T., Yaşar, D., 2002. Last glacial–Holocene paleoceanography of the Black Sea and Marmara Sea: stable isotopic, foraminiferal and coccolith evidence. Marine Geology, 190(1-2), 119-149.

Alve, E., Murray, J. W., 1994. Ecology and taphonomy of benthic foraminifera in a temperate mesotidal inlet. The Journal of Foraminiferal Research, 24(1), 18-27.

Antonarakou, A., Kontakiotis, G., Vasilatos, C., Besiou, E., Zarkogiannis, S., Drinia, H., Mortyn, P.G., Tsaparas, N., Makri, P., Karakitsios, V., 2019. Evaluating the effect of marine diagenesis on

Late Miocene pre-evaporitic sedimentary successions of eastern Mediterranean Sea. IOP Conference Series: Earth and Environmental Sciences, 221, 012051.

Archer, D., Maier-Reimer, E., 1994. Effect of deep-sea sedimentary calcite preservation on atmospheric CO_2 concentration. Nature, 367(6460), 260-263.

Archer, D., 2003. Biological Fluxes in the Ocean and Atmospheric pCO_2. Treatise on Geochemistry, 6, 625.

Auer, G., Piller, W.E., Harzhauser, M., 2014. High-resolution calcareous nannoplankton palaeoecology as a proxy for small-scale environmental changes in the Early Miocene. Marine Micropaleontology, 111, 53–65.

Baggley, K.A., 2000. The late Tortonian-early Messinian foraminiferal record of the Abad Member (Turre formation), Sorbas Basin, Almeria, south-east Spain. Palaeontology, 43, 1069–1111.

Barmawidjaja, D. M., Jorissen, F. J., Puskaric, S. V., Van der Zwaan, G. J., 1992. Microhabitat selection by benthic foraminifera in the northern Adriatic Sea. The Journal of Foraminiferal Research, 22(4), 297-317.

Blanc-Valleron, M.M., Pierre, C., Caulet, J.P., Caruso, A., Rouchy, J.M., Cespuglio, G., Sprovieri, R., Pestrea, S., Di Stefano, E., 2002. Sedimentary, stable isotope and micropaleontological records of paleoceanographic change in the Messinian Tripoli Formation (Sicily, Italy). Palaeogeography, Palaeoclimatology, Palaeoecology, 185, 255–286.

Bond, D. P., Wignall, P. B., 2010. Pyrite framboid study of marine Permian–Triassic boundary sections: a complex anoxic event and its relationship to contemporaneous mass extinction. GSA Bulletin, 122(7-8), 1265-1279.

Bots, P., Benning, L. G., Rickaby, R., Shaw, S., 2011. The role of SO_4 in the switch from calcite to aragonite seas. Geology, 39(4), 331-334.

Bourillot, R., Vennin, E., Rouchy, J.M., Durlet, C., Rommevaus, V., Kolodka, C., Knap, F., 2009. Structure and evolution of a Messinian mixed carbonate-siliciclastic platform: the role of evaporites (Sorbas Basin, South-east Spain). Sedimentology 57, 477–512.

Bown, P.R., Young, J.R., 1998. Techniques. In: Bown, P.R., Ed., Calcareous nannofossil biostratigraphy, Chapman and Hall, London, 16-28.

Braga, J.C., Martin, J.M., Riding, R., Aguirre, J., Sanchez-Almazo, I.M., Dinares-Turell, J., 2006. Testing models for the Messinian salinity crisis: the Messinian record in Almeria, SE Spain. Sedimentary Geology, 188, 131–154.

Bulian, F., Kouwenhoven, T. J., Jiménez-Espejo, F. J., Krijgsman, W., Andersen, N., Sierro, F. J., 2022. Impact of the Mediterranean-Atlantic connectivity and the late Miocene carbon shift on deep-

753 sea communities in the Western Alboran Basin. Palaeogeography, Palaeoclimatology, Palaeoecology,
754 110841.

755 Buckman, J., Mahoney, C., März, C., Wagner, T., 2020. The Secret 'After Life' of Foraminifera: Big
756 Things Out of Small. Minerals, 10(6), 550.

757 Burton, E.A., Walter, L.M., 1991, The effects of pCO_2 and temperature on magnesium incorporation
758 in calcite in seawater and $MgCl_2$- $CaCl_2$ solutions: Geochimica et Cosmochimica Acta, 55, 777–785.

759 Buzas-Stephens, P., Buzas, M. A., 2005. Population dynamics and dissolution of foraminifera in
760 Nueces Bay, Texas. The Journal of Foraminiferal Research, 35(3), 248-258.

761 Carnevale, G., Gennari, R., Lozar, F., Natalicchio, M., Pellegrino, L., Dela Pierre, F., 2019. Living in
762 a deep desiccated Mediterranean Sea: an overview of the Italian fossil record of the Messinian salinity
763 crisis. Bollettino della Società Paleontologica Italiana, 58, 109–140.

764 Capella, W., Barhoun, N., Flecker, R., Hilgen, F. J., Kouwenhoven, T., Matenco, L. C., Sierro, F.J.,
765 Tulbure, M.A., Yousfi, M.Z., Krijgsman, W., 2018. Palaeogeographic evolution of the late Miocene
766 Rifian Corridor (Morocco): reconstructions from surface and subsurface data. Earth-Science
767 Reviews, 180, 37-59.

768 Catalano R., Di Stefano E., Sprovieri R., Lena G., Valenti V., 2016. The barren Messinian Tripoli in
769 Sicily and its palaeoenvironmental evolution: suggestions on the exploration potential. Petroleum
770 Geosciences, 22, 322-332

771 Chiu, T. C., Broecker, W. S., 2008. Toward better paleocarbonate ion reconstructions: New insights
772 regarding the $CaCO_3$ size index. Paleoceanography, 23(2).

773 Clauzon, G., Suc, J.P., Do Couto, D., Jouannic, G., Melinte-Dobrinescu, M.C., Jolivet, L., Martinell,
774 J., 2015. New insights on the Sorbas Basin (SE Spain): the onshore reference of the Messinian salinity
775 crisis Marine and Petroleum Geology 66, 71–100.

776 Corbi, H., Lancis, C., Giannetti, A., Tent-Manclus, J.E., Dinares- Turell, J., 2016. Sedimentological
777 and paleoenvironmental scenario before, during, and after the Messinian Salinity Crisis: the San
778 Miguel de Salinas composite section (western Mediterranean). Marine Geology 379, 246–266.

779 Corbí, H., Soria, J.M., 2016. Late Miocene–early Pliocene planktonic foraminifer event-stratigraphy
780 of the Bajo Segura basin: a complete record of the western Mediterranean. Marine and Petroleum
781 Geology, 77, 1010–1027.

782 Corbí, H., Soria, J. M., Giannetti, A., Yébenes, A., 2020. The step-by-step restriction of the
783 Mediterranean (start, amplification, and consolidation phases) preceding the Messinian Salinity Crisis
784 (climax phase) in the Bajo Segura basin. Geo-Marine Letters, 40(3), 341-361.

Dela Pierre, F., Clari, P., Natalicchio, M., Ferrando, S., Giustetto, R., Lozar, F., Lugli, S., Manzi, V., Roveri, M., Violanti, D., 2014. Flocculent layers and bacterial mats in the mudstone interbeds of the primary lower Gypsum unit (Tertiary Piedmont basin, NW Italy): archives of palaeoenvironmental changes during the Messinian salinity crisis. Marine Geology, 355, 71–87.

Dimiza, M. D., Koukousioura, O., Michailidis, I., Dimou, V. G., Navrozidou, V., Aligizaki, K., Seferlis, M., 2020. Seasonal living coccolithophore distribution in the enclosed coastal environments of the Thessaloniki Bay (Thermaikos Gulf, NW Aegean Sea). Revue de Micropaléontologie, 69, 100449.

Drinia, H., Antonarakou, A., Tsaparas, N., Kontakiotis, G., 2007. Palaeoenvironmental conditions preceding the Messinian Salinity Crisis: A case study from Gavdos Island. Geobios, 40, 251-265.

Dronkert, H., 1976. Late Miocene evaporites in the Sorbas Basin and adjoining areas. Memorie della Società Geologica Italiana, 341–361.

Flecker, R., Krijgsman, W., Capella, W., de Castro Martins, C., Dmitrieva, E., Mayser, J.P., Marzocchi, A., Modestou, S., Ochoa, D., Simon, D., Tulbure, M., van den Berg, B., van der Schee, M., de Lange, G., Ellam, R., Govers, R., Gutjahr, M., Hilgen, F., Kouwenhoven, T., Lofi, J., Meijer, P., Sierro, F.J., Bachiri, N., Barhoun, N., Alami, A.C., Chacon, B., Flores, J.A., Gregory, J., Howard, J., Lunt, D., Ochoa, M., Pancost, R., Vincent, S., Yousfi, M.Z., 2015. Evolution of the Late Miocene Mediterranean- Atlantic gateways and their impact on regional and global environmental change. Earth Science Review, 150, 365–392.

Fortuin, A. R., Krijgsman, W., 2003. The Messinian of the Nijar Basin (SE Spain): sedimentation, depositional environments and paleogeographic evolution. Sedimentary Geology, 160(1-3), 213-242.

Gavrilova, N., Dolan, J., 2007. A note on species lists and ecosystem shifts: Black Sea tintinnids, ciliates of the microzooplankton. Acta Protozoologica, 46, 279-288.

Gennari, R., Manzi, V., Angeletti, L., Bertini, A., Biffi, U., Ceregato, A., Faranda, C., Gliozzi, E., Lugli, S., Menichetti, E., Rosso, A., Roveri, M., Taviani, M., 2013. A shallow water record of the onset of the Messinian salinity crisis in the Adriatic foredeep (Legnagnone section, Northern Apennines). Palaeogeography, Palaeoclimatology, Palaeoecology, 386, 145-164.

Gennari, R., Lozar, F., Turco, E., Dela Pierre, F., Manzi, V., Natalicchio, M., Lugli, S., Roveri, M., Schreiber, B.C., Taviani, M., 2018. Integrated stratigraphy and paleoceanographic evolution of the pre-evaporitic phase of the Messinian salinity crisis in the Eastern Mediterranean as recorded in the Tokhni section (Cyprus island). Newsletters on Stratigraphy, 51, 33–55.

Gennari, R., Lozar, F., Natalicchio M., Zanella, E., Carnevale, G., Dela Pierre, F., 2020. Chronology of the Messinian events in the northernmost part of the Mediterranean: the Govone section (Piedmont Basin, NW Italy). Rivista Italiana di Paleontologia e Stratigrafia, 126, 517–60.

Gibbs, S., Shackleton, N., Young, J.R., 2004. Orbitally forced climate signals in mid- Pliocene nannofossil assemblages. Marine Micropaleontology, 51, 39–56.

Giraudeau, J., 1992. Distribution of recent nannofossils beneath the Benguela system: southwest African continental margin. Marine Geology 108, 219–237.

Goubert, E., Néraudeau, D., Rouchy, J. M., Lacour, D., 2001. Foraminiferal record of environmental changes: Messinian of the Los Yesos area (Sorbas Basin, SE Spain). Palaeogeography, Palaeoclimatology, Palaeoecology, 175(1-4), 61-78.

Hsü, K.J., Montadert, L., Bernoulli, D., Cita, M.B., Erikson, A., Garrison, R.E., Kidd, R.B., Mélières, F., Muller, C., Wright, R.H., 1977. History of the Mediterranean salinity crisis. Nature, 267(5610), 399-403.

Jahnke, R. A., Craven, D. B., McCorkle, D. C., Reimers, C. E., 1997. $CaCO_3$ dissolution in California continental margin sediments: The influence of organic matter remineralization. Geochimica et Cosmochimica Acta, 61(17), 3587-3604.

Karakitsios, V., Roveri, M., Lugli, S., Manzi, V., Gennari, G., Antonarakou, A., Triantaphyllou, M., Agiadi, K., Kontakiotis, G., Kafousia, N., de Rafelis, M., 2017. A record of the Messinian salinity crisis in the eastern Ionian tectonically active domain (Greece, eastern Mediterranean). Basin Research 29, 203–233.

Kontakiotis, G., Besiou, E., Antonarakou, A., Zarkogiannis, S., Kostis, A., Mortyn, P.G., Moissette, P., Cornée, J.J., Schulbert, C., Drinia, H., Anastasakis, G., Karakitsios,V., 2019. Decoding sea surface and paleoclimate conditions in the eastern Mediterranean over the Tortonian-Messinian Transition. Palaeogeography, Palaeoclimatology, Palaeoecology, 534, 109312.

Kontakiotis, G., Karakitsios, V., Cornée, J., Moissette, P., Zarkogiannis, S.D., Pasadakis, N., Koskeridou, E., Manoutsoglou, E., Drinia, H., Antonarakou, A., 2020. Preliminary results based on geochemical sedimentary constraints on the hydrocarbon potential and depositional environment of a Messinian sub-salt mixed siliciclastic-carbonate succession onshore Crete (Plouti section, eastern Mediterranean). Mediterranean Geoscience Review, 2, 247-265.

Kontakiotis, G., Karakitsios, V., Maravelis, A.G, Zarkogiannis, S.D., Agiadi, K., Antonarakou, A., Pasadakis, N., Zelilidis, A., 2021. Integrated isotopic and organic geochemical constraints on the depositional controls and source rock quality of the Neogene Kalamaki sedimentary successions (Zakynthos Island, Ionian Sea). Mediterranean Geoscience Review, 3,193–217.

Kontakiotis, G., Butiseacă, G. A., Antonarakou, A., Agiadi, K., Zarkogiannis, S. D., Krsnik, E., Besiou, E., Zachariasse, W.J., Lourens, L., Thivaiou, D., Kosteridou, E., Moisette, P., Mulch, A., Karakitsios, V., Vasiliev, I., 2022. Hypersalinity accompanies tectonic restriction in the eastern

852 Mediterranean prior to the Messinian Salinity Crisis. Palaeogeography, Palaeoclimatology,
853 Palaeoecology, 592, 110903.

854 Kouwenhoven, T.J., Seidenkrantz, M.S., van der Zwaan, G.J., 1999. Deep-water changes: the near
855 synchronous disappearance of a group of benthic foraminifera from the Late Miocene Mediterranean.
856 Palaeogeography, Palaeoclimatology, Palaeoecology. 152, 259–281.

857 Kouwenhoven, T.J., Morigi, C., Negri, A., Giunta, S., Krijgsman, W., Rouchy, J.M., 2006.
858 Palaeoenvironmental evolution of the eastern Mediterranean during the Messinian: constraints from
859 integrated microfossil data of the Pissouri Basin (Cyprus). Marine Micropaleontology, 60, 17–44.

860

861 Krijgsman, W., Hilgen, F. J., Raffi, I., Sierro, F. J., Wilson, D. S., 1999. Chronology, causes and
862 progression of the Messinian salinity crisis. Nature, 400(6745), 652-655.

863 Krijgsman, W., Fortuin, A. R., Hilgen, F. J., Sierro, F. J., 2001. Astrochronology for the Messinian
864 Sorbas basin (SE Spain) and orbital (precessional) forcing for evaporite cyclicity. Sedimentary
865 Geology, 140(1-2), 43-60.

866 Krijgsman, W., Leewis, M. E., Garcés, M., Kouwenhoven, T. J., Kuiper, K. F., Sierro, F. J., 2006.
867 Tectonic control for evaporite formation in the Eastern Betics (Tortonian; Spain). Sedimentary
868 Geology, 188, 155-170.

869 Kubryakov, A. A., Mikaelyan, A. S., Stanichny, S. V., 2021. Extremely strong coccolithophore
870 blooms in the Black Sea: The decisive role of winter vertical entrainment of deep water. Deep Sea
871 Research Part I: Oceanographic Research Papers, 173, 103554.

872 Lacour, D., Nèraudeau, D., 2000. Évolution de la diversité des *Brissopsis* intragypses de Sorbas (SE
873 Espagne). Geodiversitas, 22(4), 509-523.

874 Landini W., Sorbini L., 1989. Ichthyofauna of the evaporitic Messinian in the Romagna and Marche
875 regions. Bollettino della Società Paleontologica Italiana, 28, 287-293.

876 Larson, E. B., Mylroie, J. E., 2014. A review of whiting formation in the Bahamas and new
877 models. Carbonates and Evaporites, 29(4), 337-347.

878 Lee, D., Carpenter, S. J., 2001. Isotopic disequilibrium in marine calcareous algae. Chemical
879 geology, 172(3-4), 307-329.

880 Lirer, F., Foresi, L. M., Iaccarino, S. M., Salvatorini, G., Turco, E., Cosentino, C., Sierro, F.J., Caruso,
881 A., 2019. Mediterranean Neogene planktonic foraminifer biozonation and biochronology. Earth-
882 Science Reviews, 196, 102869.

883 Liu, X., Li, A., Dong, J., Zhuang, G., Xu, F., Wan, S., 2018. Nonevaporative origin for gypsum in
884 mud sediments from the East China Sea shelf. Marine Chemistry, 205, 90-97.

Loreau, J.P., 1982, Sediments aragonitiques et leur denise: Memoires du Museum National d'Histoire Naturelle, Serie C., Tome XLVI1, 300 p.

Lozar, F., Violanti, D., Bernardi, E., Dela Pierre, F., Natalicchio, M., 2018. Identifying the onset of the Messinian salinity crisis: a reassessment of the biochronostratigraphic tools (Piedmont Basin, NW Italy). Newsletter on Stratigraphy 51(1), 11–31.

Lozar, F., Negri, A., 2019. A review of basin-wide calcareous nannofossil bioevents in the Mediterranean at the onset of the Messinian salinity crisis. Marine Micropaleontology 151, 101752.

Lugli, S., Manzi, V., Roveri, M., Schreiber, B. C., 2010. The Primary Lower Gypsum in the Mediterranean: a new facies interpretation for the first stage of the Messinian salinity crisis. Palaeogeography, Palaeoclimatology, Palaeoecology, 297, 83–99.

Macintyre I. G., Reid R.P., 1992. Comment on the origin of aragonite needle mud: a picture is worth a thousand words. Journal of Sedimentary Petrology 62,1095–1097.

Macintyre, I. G., Reid, R. P., 1995. Crystal alteration in a living calcareous alga (*Halimeda*); implications for studies in skeletal diagenesis. Journal of Sedimentary Research, 65(1a), 143-153.

Mancini, A. M., Gennari, R., Ziveri, P., Mortyn, P. G., Stolwijk, D. J. Lozar, F., 2020. Calcareous nannofossil and foraminiferal trace element records in the Sorbas Basin: A new piece of the Messinian Salinity Crisis onset puzzle. Palaeogeography, Palaeoclimatology, Palaeoecology, 554, 109796.

Mancini, A. M., Grelaud, M., Ziveri, P., Nallino, E., Lozar, F., 2021. Calcareous nannofossil size and abundance response to the Messinian Salinity Crisis onset and paleoenvironmental dynamics. Paleoceanography and Paleoclimatology, 36(9), e2020PA004155.

Manzi, V., Roveri, M., Gennari, R., Bertini, A., Biffi, U., Giunta, S., Iaccarino, S.M., Lanci, L., Lugli, S., Negri, A., Riva, A., Rossi, M.E., Taviani, M., 2007. The deep-water counterpart of the Messinian Lower Evaporites in the Apennine foredeep: the Fanantello section (Northern Apennines, Italy). Palaeogeography, Palaeoclimatology, Palaeoecology. 251, 470–499.

Manzi, V., Gennari, R., Hilgen, F., Krijgsman, W., Lugli, S., Roveri, M., Sierro, F.J., 2013. Age refinement of the Messinian salinity crisis onset in the Mediterranean. Terra Nova 25, 315–322.

Manzi, V., Gennari, R., Lugli, S., Minelli, N., Reghizzi, M., Roveri, M., Schreiber, B. C., 2016. Comment on “Carbonate deposition and diagenesis in evaporitic environments: The evaporative and sulphur-bearing limestones during the settlement of the Messinian Salinity Crisis in Sicily and Calabria” by Caruso et al., 2015. Palaeo3, 429, 136–162. Palaeogeography, Palaeoclimatology, Palaeoecology, 459, 585-596.

Manzi, V., Gennari, R., Lugli, S., Persico, D., Reghizzi, M., Roveri, M., Schreiber, B. C., Calvo, R., Gavrieli, I., Gvirtzman, Z., 2018. The onset of the Messinian salinity crisis in the deep Eastern Mediterranean basin. Terra Nova, 30(3), 189-198.

Mayser, J. P., Flecker, R., Marzocchi, A., Kouwenhoven, T. J., Lunt, D. J., Pancost, R. D., 2017. Precession driven changes in terrestrial organic matter input to the Eastern Mediterranean leading up to the Messinian Salinity Crisis. Earth and Planetary Science Letters, 462, 199-211.

Mazumder, A., Nigam, R., 2014. Bathymetric preference of four major genera of rectilinear benthic foraminifera within oxygen minimum zone in Arabian Sea off central west coast of India. Journal of Earth System Science, 123(3), 633-639.

McNeil, D. H., 1997. Diagenetic regimes and the foraminiferal record in the Beaufort-Mackenzie Basin and adjacent cratonic areas. Annales Societatis Geologorum Poloniae, 67(2-3), 271-286.

Meier, K. S., Kinkel, H., Young, J., 2014. A note on calcareous nannoplankton from the Kieler Förde (Baltic Sea). Journal of Nannoplankton Research, 33, 29-37.

Milliman, J. D., 1974. Precipitation and cementation of deep-sea carbonate sediments. Deep-Sea Sediments (463-476). Springer, Boston, MA.

Milliman, J.D., Freile, D., Steinen, R.P. Wilber, R.J., 1993. Great Bahama Bank aragonitic muds: mostly inorganically precipitated, mostly exported. Journal of Sedimentary Petrology, 63, 589–595.

Modestou, S., Simon, D., Gutjahr, M., Marzocchi, A., Kowenhoven, T.J., Ellam, R.M., Flecker, R., 2017. Precessional variability of 87Sr/86Sr in the late Miocene Sorbas Basin: an interdisciplinary study of drivers of interbasin exchange. Paleoceanography, 32, 1–22.

Moissette, P., Cornée, J.- J., Antonarakou, A., Kontakiotis, G., Drinia, H., Koskeridou, E., Tsourou, T., Agiadi, K., Karakitsios, V., 2018. Palaeoenvironmental changes at the Tortonian/Messinian boundary: A deep-sea sedimentary record of the eastern Mediterranean Sea. Palaeogeography, Palaeoclimatology, Palaeoecology, 505, 217-233.

Montenat, C., Ott d'Estevou, P., Plaziat, J. C., Chapel, J., 1980. La signification des faunes marines contemporaines des évaporites messiniennes dans le Sud-Est de l'Espagne. Conséquences pour l'interprétation des conditions d'isolement de la Méditerranée occidentale. Géologie méditerranéenne, 7(1), 81-89.

Morse, J. W., Wang, Q., Tsio, M. Y., 1997. Influences of temperature and Mg:Ca ratio on $CaCO_3$ precipitates from seawater. Geology, 25(1), 85-87.

Murray, J. W., 2006. Ecology and applications of benthic foraminifera. Cambridge University Press.

Natalicchio, M., Dela, Pierre F., Birgel, D., Brumsack, H., Carnevale, G., Gennari, R., Gier, S., Lozar, F., Pellegrino, L., Sabino, M., Schnetger, B., Peckmann, J., 2019. Paleoenvironmental change in a

precession-paced succession across the onset of the Messinian salinity crisis: Insight from element geochemistry and molecular fossils. Palaeogeography, Palaeoclimatology, Palaeoecology, 518, 45–61.

Néraudeau D., Videt B., Courville P., Goubert E., Rouchy J.-M., 2002. Corrélation des niveaux fossilifères marins interstratifés dans les gypses messiniens, entre la carrière de Molinos de Aguas (bassin de Sorbas, SE Espagne). Geodiversitas, 24, 659-667.

Obst, M., Dynes, J., Lawrence, J., Swerhone, G., Benzerara, K., Karunakaran, C., Kaznatcheev K., Tyliszczak, T., Hitchcock A.P., 2009. Precipitation of amorphous $CaCO_3$ (aragonite-like) by cyanobac-teria: a STXM study of the influence of EPS on the nucleation process. Geochimica Cosmochimica Acta, 73, 4180–4198.

Paasche, E., Brubak, S., Skattebøl, S., Young, J. R., Green, J. C. 1996. Growth and calcification in the coccolithophorid Emiliania huxleyi (Haptophyceae) at low salinities. Phycologia, 35(5), 394-403.

Pellegrino, L., Natalicchio, M., Abe, K., Jordan, R. W., Longo, S. E. F., Ferrando, S., Carnevale, G., Dela Pierre, F., 2021. Tiny, glassy, and rapidly trapped: The nano-sized planktic diatoms in Messinian (late Miocene) gypsum. Geology, 49(11), 1369-1374.

Perri, E., Gindre-Chanu, L., Caruso, A., Cefalà, M., Scopelliti, G., Tucker, M., 2017. Microbial-mediated pre-salt carbonate deposition during the Messinian salinity crisis (Calcare di Base fm., Southern Italy). Marine and Petroleum Geology, 88, 235-250.

Peterson, L. C., Prell, W. L., 1985. Carbonate dissolution in recent sediments of the eastern equatorial Indian Ocean: preservation patterns and carbonate loss above the lysocline. Marine Geology, 64(3-4), 259-290.

Pierre, C., 1999. The oxygen and carbon isotope distribution in the Mediterranean water masses. Marine geology, 153(1-4), 41-55.

Pierre, C., Rouchy, J. M., 2004. Isotopic compositions of diagenetic dolomites in the Tortonian marls of the western Mediterranean margins: evidence of past gas hydrate formation and dissociation. Chemical Geology, 205(3-4), 469-484.

Reghizzi, M., Gennari, R., Douville, E., Lugli, S., Manzi, V., Montagna, P., Roveri, M., Sierro, F.J., Taviani, M., 2017. Isotope stratigraphy (87Sr/86Sr, δ18O, δ13C) of the Sorbas basin (Betic Cordillera, Spain): Paleoceanographic evolution across the onset of the Messinian salinity crisis. Palaeogeography, Palaeoclimatology, Palaeoecology, 469, 60–73.

Riding, R., Braga, J.C., Martin, J.M., Sanchez-Almazo, I.M., 1998. Mediterranean Messinian salinity crisis: constraints from a coeval marginal basin, Sorbas, southeastern Spain. Marine Geology, 146, 1–20.

Robbins, L.L., Blackwelder, P.L., 1992. Biochemical and ultrastructural evidence for the origin of whitings: a biologically induced calcium carbonate precipitation mechanism. Geology 20, 464–468.

Roep, T. B., Dabrio, C. J., Fortuin, A. R., Polo, M. D., 1998. Late highstand patterns of shifting and stepping coastal barriers and washover-fans (late Messinian, Sorbas Basin, SE Spain). Sedimentary Geology, 116, 27–56.

Roth, P. H., Berger, W. H., 1975. Distribution and dissolution of coccoliths in the South and central Pacific, Foraminiferal Research, 13, 87–113.

Roth, P. H., Coulbourn, W. T., 1982. Floral and solution patterns of coccoliths in surface sediments of the North Pacific, Marine Micropaleontology, 7, 1– 52.

Rouchy, J. M., Caruso, A., 2006. The Messinian salinity crisis in the Mediterranean basin: a reassessment of the data and an integrated scenario. Sedimentary Geology, 188, 35-67.

Roveri, M., Gennari, R., Lugli, S., Manzi, V., 2009. The Terminal Carbonate Complex: the record of sea-level changes during the Messinian salinity crisis. GeoActa 8, 57–71.

Roveri, M., Flecker, R., Krijgsman, W., Lofi, J., Lugli, S., Manzi, V., Sierro, F.J., Bertini, A., Camerlenghi, A., De Lange, G., Govers, R., Hilgen, F.J., Hubscher, C., Meijer, P.T., Stoica, M., 2014. The Messinian Salinity Crisis: past and future of a great challenge for marine sciences. Marine Geology, 352, 25–58.

Roveri, M., Gennari, R., Persico, D., Rossi, F. P., Lugli, S., Manzi, V., Reghizzi, M., Taviani, M., 2019. A new chronostratigraphic and palaeoenvironmental framework for the end of the Messinian salinity crisis in the Sorbas Basin (Betic Cordillera, southern Spain). Geological Journal, 54(3), 1617-1637.

Roveri, M., Lugli, S., Manzi, V., Reghizzi, M., Rossi, F. P., 2020. Stratigraphic relationships between shallow-water carbonates and primary gypsum: insights from the Messinian succession of the Sorbas Basin (Betic Cordillera, Southern Spain). Sedimentary Geology, 404, 105678.

Ruegg, G. J. H., 1964. Geologische onderzoekingen in het bekken van Sorbas, S Spanje. Amsterdam Geological Institut, University of Amsterdam, 64.

Sabino, M., Schefuß, E., Natalicchio, M., Dela Pierre, F., Birgel, D., Bortels, D., Schnetger, B., Peckmann, J., 2020. Climatic and hydrologic variability in the northern Mediterranean across the onset of the Messinian salinity crisis. Palaeogeography, Palaeoclimatology, Palaeoecology, 545, 109632.

Saint Martin, J. P., Pestrea, S., Conesa, G., 2001. Les assemblages de diatomées des niveaux infra-gypseux du bassin messinien de Sorbas (Espagne). Cryptogamie Algologie, 22(1), 127-149.

Sakka, A., Legendre, L., Gosselin, M., LeBlanc, B., Delesalle, B., Price, N. M., 1999. Nitrate, phosphate, and iron limitation of the phytoplankton assemblage in the lagoon of Takapoto Atoll (Tuamotu Archipelago, French Polynesia). Aquatic Microbial Ecology, 19(2), 149-161.

Schiebel, R., Hemleben, C., 2017. Planktic foraminifers in the modern ocean. Berlin, Springer, 1-358.

Shinn, E.A., Steinen, R.P., Lidz, B.H. Swart, P.K., 1989. Whitings, a sedimentologic dilemma. Journal of Sedimentary Petrology, 59, 147– 161.

Sierro, F.J., Hilgen, F.J., Krijgsman, W., Flores, J.A., 2001. The Abad composite (SE Spain): a Mediterranean and global reference section for the Messinian. Palaeogeography, Palaeoclimatology, Palaeoecology, 168, 141–169.

Sierro, F.J., Flores, J.A., Bàrcena, M.A., Vazquez, A., Utrilla, R., Zamarreno, I., 2003. Orbitally-controlled oscillations in the planktic communities and cyclical changes in western Mediterranean hydrography during the Messinian. Palaeogeography, Palaeoclimatology, Palaeoecology, 190, 289–316

Silva, A., Palma, S., Moita, M.T., 2008. Coccolithophores in the upwelling waters of Portugal: four years of weekly distribution in Lisbon bay. Continental Shelf Research, 28, 2601–2613.

Sondi, I., Juračić, M., 2010. Whiting events and the formation of aragonite in Mediterranean Karstic Marine Lakes: new evidence on its biologically induced inorganic origin. Sedimentology, 57(1), 85-95.

Sprovieri, R., Di Stefano, E., Sprovieri, M., 1996. High resolution chronology for Late Miocene Mediterranean stratigraphic events. Rivista Italiana di Paleontologia e Stratigrafia, 102, 77–104.

Steinsund, P. I., Hald, M., 1994. Recent calcium carbonate dissolution in the Barents Sea: Paleoceanographic applications. Marine Geology, 117(1-4), 303-316.

Suárez-Ibarra, J. Y., Frozza, C. F., Palhano, P. L., Petró, S. M., Weinkauf, M. F., Pivel, M. A., 2022. Calcium carbonate dissolution triggered by high productivity during the last glacial-interglacial interval at the deep western South Atlantic. Frontiers in Earth Science, 10, 830984.

Subhas, A. V., Rollins, N. E., Berelson, W. M., Erez, J., Ziveri, P., Langer, G., Adkins, J. F., 2018. The dissolution behavior of biogenic calcites in seawater and a possible role for magnesium and organic carbon. Marine Chemistry, 205, 100-112.

Swart, P. K., 1983. Carbon and oxygen isotope fractionation in scleractinian corals: a review. Earth-science reviews, 19(1), 51-80.

Swart, P.K. Eberli, G.P., 2005. The nature of the δ ^{13}C of periplatform sediments: implications for stratigraphy and the global carbon cycle. Sedimentary Geology, 175, 115–130.

Swart, P.K., Reijmer, J.J. Otto, R., 2009. A re evaluation of facies on Great Bahama Bank II: variations in the δ^{13}C, δ ^{18}O and mineralogy of surface sediments. In: Perspectives in Carbonate Geology: A Tribute to the Career of Robert Nathan Ginsburg, IAS Special Publication (Eds P.K. Swart, G.P. Eberli and J.A. McKenzie), 41, 47–60. Wiley- Blackwell, Oxford

Tagliavento M., Lauridsen, B. W., Stemmerik, L., 2020. Episodic dysoxia during Late Cretaceous cyclic chalk-marl deposition – Evidence from framboidal pyrite distribution in the upper Maastrichtian Rørdal Mb., Danish Basin. Cretaceous Research 106, 104223.

Trenkwalder S., Violanti D., d'Atri A., Lozar F., Dela Pierre F., Irace A., 2008. The Miocene/Pliocene boundary and the Early Pliocene micropaleontological record: new data from the Tertiary Piedmont Basin (Moncucco quarry, Turin Hill, Northwestern Italy). Bollettino della Società Paleontologica Italiana, 47 (2), 87-103.

Troelstra, S.R., Van der Poel, H.M., Huisman, C.H.A., Geerlings, L.P.A., Dronkert, H., 1980. Paleoecological changes in the latest Miocene of the Sorbas Basin, S.E. Spain. Geologie Méditerranéenne. 8, 115–126.

Turpin, M., Emmanuel, L., Reijmer, J. J., Renard, M. 2011. Whiting-related sediment export along the Middle Miocene carbonate ramp of Great Bahama Bank. International Journal of Earth Sciences, 100(8), 1875-1893.

Tyrrell, T., Schneider, B., Charalampopoulou, A., Riebesell, U., 2008. Coccolithophores and calcite saturation state in the Baltic and Black Seas. Biogeosciences, 5(2), 485-494.

van de Poel, H. M., 1992. Foraminiferal biostratigraphy and palaeoenvironments of the Miocene-Pliocene Carboneras-Nijar basin (SE Spain). Scripta Geologica, 102, 1-32.

Vasiliev, I., Karakitsios, V., Bouloubassi, I., Agiadi, K., Kontakiotis, G., Antonarakou, A., Triantaphyllou, M., Gogou, A., Kafousia, N., de Rafélis, M., Zarkogiannis, S., Kaczmar, F., Parinos, C., Pasadakis, N., 2019. Large sea surface temperature, salinity, and productivity-preservation changes preceding the onset of the Messinian Salinity Crisis in the eastern Mediterranean Sea. Paleoceanography and Paleoclimatology, 34(2), 182-202.

Violanti D., Lozar F., Dela Pierre F., Natalicchio M., Bernardi E., Clari P. Cavagna S., 2013. Stress-tolerant microfossils of a Messinian succession from the Northern Mediterranean basin (Pollenzo section, Piedmont, northwestern Italy). Bollettino della Società Paleontologica Italiana, 52, 45-54.

Volk, H.R., Rondeel, H.E., 1967. Zur gliederung des Jungtertiärs in becken von Vera, Südost Spanien. Geologie en Mijnbouw 43, 310-315.

Weber, J. N., Raup, D. M., 1966. Fractionation of the stable isotopes of carbon and oxygen in marine calcareous organisms—the Echinoidea. Part I. Variation of ^{13}C and ^{18}O content within individuals. Geochimica et Cosmochimica Acta, 30(7), 681-703.

Wylezich, C., Jürgens, K., 2011. Protist diversity in suboxic and sulfidic waters of the Black Sea. Environmental microbiology, 13(11), 2939-2956.

Yates K. K., Robbins, L. L., 1998. Production of carbonate sediments by unicellular green alga. American Mineralogist, 83,1503–1509.

Zachariasse, W. J., Kontakiotis, G., Lourens, L. J., Antonarakou, A., 2021. The Messinian of Agios Myron (Crete, Greece): A key to better understanding diatomite formation south of Crete, on Gavdos Island. Palaeogeography, Palaeoclimatology, Palaeoecology, 581, 110633.

Ziegenbalg, S.B., Brunner, B., Rouchy, J.M., Birgel, D., Pierre, C., Böttcher, M.E., Caruso, A., Immenhauser, A., Peckmann, J., 2010. Formation of secondary carbonates and native sulphur in sulphate-rich Messinian strata, Sicily. Sedimentary Geology, 227, 37-50.